Properties and stratigraphy of polar ice patches in the Canadian High Arctic reveal their current resilience to warm summers

Gautier Davesne, Daniel Fortier, Florent Domine

Canadian Science Publishing

ARTICLE

Properties and stratigraphy of polar ice patches in the Canadian High Arctic reveal their current resilience to warm summers[1]

Gautier Davesne, Daniel Fortier, and Florent Domine

Abstract: Ice patches are ubiquitous in polar regions and are a key element for landscape evolution. We present new insights into polar desert ice patch formation based on snow and ice properties at Ward Hunt Island (Canadian High Arctic, 83°N). Our results demonstrate that ice patches are composed of two distinct units. The upper unit is characterized by very fine granular and bubbly ice with a clear oblique layering. By contrast, the lower unit is strikingly different with coarse crystals, lower porosity, and a high frequency of fractures. For both units, superimposed ice formation at the base of the deep snowpack stands out as the primary ice aggradation process. The distinct properties of the lower unit likely result from a long period of kinetic ice crystal growth indicating a minimum age of several hundred years. A radiocarbon date of 3 487 ± 20 cal BP suggests that ice patches could potentially date back to the late Holocene. This old ice was recently truncated during warmer summers between 2008 and 2012, but the ice patch quickly recovered its volume during cooler summers. The old age of the ice patches and their rapid regeneration after melt events suggest their resilience to current warmer summers.

Key words: ice patch, polar desert, climate change, snowpack, slope hydrology.

Résumé : Les plaques de glace sont omniprésentes dans les régions polaires et constituent un élément clé de l'évolution du paysage. Les auteurs présentent de nouvelles connaissances sur la formation des plaques de glace dans les déserts polaires, basées sur les propriétés de la neige et de la glace à l'île Ward Hunt (Haut-Arctique canadien, 83°N). Leurs résultats démontrent que les plaques de glace sont composées de deux unités distinctes. L'unité supérieure est caractérisée par une glace très fine, granuleuse et bouillonnante, avec une stratification oblique claire. En revanche, l'unité inférieure est étonnamment différente avec des cristaux grossiers, une porosité plus faible et une fréquence élevée de fractures. Pour les deux unités, la formation de glace superposée à la base du manteau neigeux profond ressort comme le principal processus d'aggradation de la glace. Les propriétés distinctes de l'unité inférieure résultent probablement d'une longue période de croissance cinétique des cristaux de glace indiquant un âge minimum de plusieurs centaines d'années. Une date radiocarbone de 3487 ± 20 cal BP suggère que les plaques de glace pourraient potentiellement remonter à l'Holocène tardif. Cette vieille glace a récemment été tronquée pendant les étés plus chauds entre 2008 et 2012, mais la plaque de glace a

Received 13 February 2021. Accepted 17 September 2021.

G. Davesne and D. Fortier. Cold Regions Geomorphology and Geotechnical Laboratory, Département de géographie, Université de Montréal, Montréal, QC H3T 1J4, Canada; Centre for Northern Studies, Université Laval, Québec, QC G1V 0A6, Canada.
F. Domine. Takuvik Joint International Laboratory, Université Laval, Québec, QC G1V 0A6, Canada; CNRS-INSU (France), Département de chimie and Centre for Northern Studies, Université Laval, Québec, QC G1V 0A6, Canada.
Corresponding author: Gautier Davesne (email: gautier.davesne@umontreal.ca).
[1]This article is part of a Virtual Special Issue entitled: Terrestrial Geosystems, Ecosystems, and Human Systems in the Fast-Changing Arctic.

rapidement récupéré son volume pendant les étés plus frais. Le stade de vieillesse des plaques de glace et leur régénération rapide après les événements de fonte suggèrent leur résilience aux étés plus chauds actuels. [Traduit par la Rédaction]

Mots-clés : banquise, désert polaire, changement climatique, manteau neigeux, hydrologie des pentes.

Introduction

The cryosphere includes the terrestrial, freshwater, and oceanic systems of the polar regions and plays a key role in the climate system through its influence on freshwater resources, gas fluxes, and regulation of energy at various scales (Meredith et al. 2019). In the Arctic, the long-term temperature trend shows a rapid rate of warming from 1990 to present, leading to major changes throughout the north polar cryosphere (Post et al. 2019). This results in a wide range of environmental and climatic effects, which have attracted increased attention to cryospheric features. Studies dealing with the terrestrial cryosphere have mainly considered medium-sized and large features such as ice sheets, ice caps, and glaciers. By contrast, smaller ice masses have received little scientific attention because until recently their detection by remote sensing was limited by the availability of aerial photographs or by the resolution of satellite imagery products, and field investigations were limited. Their exclusion from terrestrial cryosphere inventories and studies leads to a significant source of error, on the order of 10% in the total terrestrial ice volume (Bahr and Radić 2012; Leigh et al. 2019; Colucci et al. 2021) and to a knowledge gap regarding their dynamics, their environmental effects, and their responses to short- and long-term climate fluctuations.

The term "small ice masses" collectively describes all perennial ice bodies at the Earth's surface whose size is below the arbitrary threshold of 0.5 km^2 (Leigh et al. 2019). A wide range of definitions and terms exists, with some focusing on the ice movement, others on the size, or others on the ice origin. Small ice masses include very small glaciers, such as ice aprons, glacier niches, small cirque glaciers, and small ice caps (Haeberli et al. 2004; Cogley et al. 2011; Guillet and Ravanel 2020), and ice patches that encompass all perennial ice bodies that are not an active glacier according to the broad definition proposed by Serrano et al (2011) and Ødegård et al. (2017) to which we adhere here. Ice patches consist of thin accumulations of ice generally overlaid by firn, i.e., a metamorphized snow that survived at least one ablation season and in which the pore space is at least partially interconnected (Cogley et al. 2011). Perennial ice patches exist continuously for centuries or millennia, whereas semi-permanent ice patches persist for several consecutive years but disappear completely occasionally during warm summers (Meulendyk et al. 2012; Woo and Young 2014; Ødegård et al. 2017). They are, thus, distinguished from snow patches (also referred to as late-lying snow patches or snowbank) that melt every summer. Ice patches are, in fact, interpreted as an intermediate state in the seasonal snow patch to glacier continuum, making the semantic boundary between ice patches and very small glaciers unclear. The major criterion to differentiate an ice patch from a very small glacier is the absence of dynamic deformations and creep of the ice mass due to the low basal shear stress (Ballantyne and Benn 1994; Ødegård et al. 2017). Serrano et al (2011) distinguished two kinds of ice patches according to their origins and the resulting internal structure (i.e., ice physics and ice stratigraphy). First, "nival ice patches" refer to ice patches created by local high accumulations of snow in favourable topographic sites (e.g., concavities and break-of-slopes), either by drifting snow or avalanching. These local persistent snow accumulations gradually turn into firn and ice through thermo-physical processes, including the formation of superimposed ice in early summer and the refreezing of meltwater in

the fall (Kawashima 1993). The second ice mass type, called "glacial ice patches", refers to ice patches formed by relict glacial ice in a paraglacial landscape during a period of deglaciation. The ice physics and structure thus retain signs of past glacial dynamics (e.g., features such as the deformation of glacier banding, foliations, and closed or filled crevasses; Serrano et al. 2011). In a favourable topographical context (e.g., the bottom of a glacial cirque, or under a rock wall), glacial ice masses can be well preserved by an active snow input that leads to the development of a hybrid system in which a nival ice patch forms on a basement made of glacier ice (Gachev et al. 2016; Yamamoto and Yoshida 1987).

Despite their limited individual size, ice patches are ubiquitous, making them an important contributor to the regional and local hydrological cycle, landscape evolution, and ecosystem functioning. Across the Canadian Arctic Archipelago, where approximately 44% of the ice-free land is occupied by a polar desert ecozone (Bliss and Gold 1999), ice patches are numerous (Lauriol et al. 1986), represent an important reservoir for freshwater, and are a primary contributor to the hydrological cycle of small watersheds by sustaining meltwater flow on slopes throughout the summer (Lewkowicz and Young 1990; Paquette et al. 2018; Young et al. 2017). Their presence is associated with mass transfers on slopes, especially solifluction (Wilkinson and Bunting 1975; Christiansen 1998; Washburn 1999; Verpaelst et al. 2017) and affects the surface energy budget, the ground thermal regime (Lewkowicz and Young 1991), and biological activities, from microbes to vegetation and animals (Gooseff et al. 2003). This wide range of implications on the physical and biological environment highlights that ice patches deserve particular attention, especially in the polar desert where water supplies are strongly limited, to understand their response to climate change and to assess how such responses will impact water discharge, geochemistry, sediment fluxes on slopes, and vegetation dynamics. To achieve this, knowledge of the internal structure and basic properties of the ice (i.e., crystallography, air bubble concentration and shape, sediment inclusions) is an important prerequisite. To date, only a few glaciological investigations have been performed on ice patches and ice physics has never been investigated in detail. Most studies were undertaken in mid-latitude mountains, since the 1970s in Japan (e.g., Wakahama and Narita 1975; Yamamoto and Yoshida 1987; Kawashima 1993; Sakai et al. 2006), and more recently in Scandinavia (Hirvas et al. 2000; Ødegård et al. 2017) and in western Canada (Meulendyk et al. 2012). Specifically, in polar regions, empirical knowledge of ice patches is thus far limited to only two studies: Østrem (1963) who undertook an analysis of the ice physics of subpolar and polar ice patches in Scandinavia and on Baffin Island, and Lewkowicz and Harry (1991) who studied a polar ice patch on Melville Island in Nunavut, Canada. Both studies proposed an analysis of the internal structure through ice cores description (e.g., porosity and sediment inclusions) and isotopic composition. Despite those pioneering studies, large knowledge gaps persist regarding the properties and the formation of polar ice patches. Little is known about the different processes that lead to the formation of new ice and about the variability of the ice facies across an ice patch. Moreover, the stratigraphy and properties of preferential snow accumulation have not yet been investigated in the polar desert. As the seasonal snow represents the major input of mass to ice patch systems, snow physical properties are expected to modulate the heat and liquid water fluxes, which, in turn, control the ice growth processes.

To fill these gaps and gain a deeper understanding of the processes behind ice patch formation and its annual and pluriannual dynamic, we performed a detailed analysis of two ice patches located on Ward Hunt Island, a polar desert site situated at the northern edge of the terrestrial Canadian Arctic. This study addressed the question of how the seasonal snow properties modulate the ice formation and which thermodynamic processes are involved in the transformation of the snow to ice under polar desert conditions.

The objectives were (*i*) to characterize in detail the physical properties and metamorphic processes of the snowpack that feed the ice patches, and (*ii*) to analyze the internal ice features (ice crystallography, bubble sizes and shapes, and sediment inclusion) and structure of the ice patches. A secondary aim was to consider these ice features in the context of long-term and current climate variations, including the extreme warming that has been recorded at this site over the last decade. This research is a contribution to the project "Terrestrial Multidisciplinary distributed Observatories for the Study of Arctic Connections" (T-MOSAiC), which places emphasis on system-level properties, including responses of the cryosphere to rapid warming (Vincent et al. 2019).

Study site

Ward Hunt Island (83°05'09"N, 74°06'19"W; hereinafter: WHI) is located at the northern tip of the Canadian Arctic Archipelago (Fig. 1*a*, *b*) and is characterized by a polar desert landscape. A general description of the physiography, geomorphology, and vegetation is given by Vincent et al. (2011). The mean annual air temperature recorded at the SILA weather station (Fig. 1*c*) was –17.1 °C for the period 2005–2019 with a monthly mean ranging between –31.6 °C in February and 1.7 °C in July (CEN 2021). The melting season extends generally from mid-June to the end of August, with days below freezing where melt pauses. No long-term precipitation data are available for WHI, but are likely similar to the average of 185 mm w.e. year^{-1} measured at Alert, located 170 km to the southeast. About 90% of the total precipitation amount falls as snow (Environment and Climate Change Canada 2021). The prevailing winds blow from the south–southwest according to measurements recorded at the SILA station from 2005 to 2019. The strongest maximum hourly average wind speeds have been recorded for the alongshore westerly winds with wind speeds exceeding 20 m s^{-1} during major storms (CEN 2021). The persistence of high winds in winter leads to an important redistribution of snow across the landscape that produces large heterogeneities in snow depths that rarely exceed 40 cm on exposed terrain but can reach over 150 cm in areas of preferential accumulation (Domine et al. 2018; Davesne et al. 2021). Unlike Ellesmere Island, WHI has no glaciers but the cryosphere is omnipresent on the island and its surroundings (Fig. 1*c*). The sea channel between the south coast of the island and Ellesmere is occupied by pack ice and the remnants of the Ward Hunt Ice Shelf (WHIS) that disintegrated in summer 2011 (Copland et al. 2017). The north and west coast are bordered by the Ward Hunt Ice Rise (WHIR) (Braun et al. 2004). On the island, the largest and most conspicuous perennial ice masses are the ice patches. Most of them are found between 20 and 50 m a.s.l. along the main break-of-slope at the junction of steep faces with scree slopes below and on the leeward concave hillslopes at higher elevations (Fig. 1*c*). These ice patches play a key role as the main provider of water to the hydrological system throughout the summer, feeding the surface and subsurface drainage network, the Ward Hunt Lake and lowland wetlands. The rapid circulation of this water via water tracks favours sediment transfers and slope denudation processes (Paquette et al. 2020). Beneath the surface, WHI is characterized by cold continuous permafrost several hundred metres thick, with a mean annual temperature of –13.5 °C at 3 m depth according to the measurements provided by a thermistor cable for the period July 2015–July 2019 (CEN 2021).

Materials and methods

This study of ice patches on WHI consisted of a detailed description of (*i*) the seasonal snow accumulation that feeds the ice patches, and (*ii*) ice cores based on a combination of thin sections and tomodensitometric (CT-scan) image analysis. This study focuses on two ice patches, named IP1 (Ice patch 1) and IP2 (Ice patch 2) (Figs. 1*c* and 2). These ice patches were selected after initial field surveys and examination of a GEOEYE image taken on

Fig. 1. (*a*, *b*) Location of Ward Hunt Island (WHI) at the northern tip of Ellesmere Island; WHIS, Ward Hunt Ice Shelf; WHIR, Ward Hunt Ice Rise (delimitation of 2008; Vincent et al. 2011). (*c*) GeoEYE satellite image taken on 26 August 2011. The red squares indicate the investigated ice patch 1 (IP1) and ice patch 2 (IP2). The GeoEYE image shows the ice patches at their minimal extent at the end of the warm summer 2011, which was marked by the complete disappearance of the perennial ice cover on Ward Hunt Lake (WHL) for the first time since observations began in the 1950s (Paquette et al. 2015). Boundary polygon in (*a*) was from the Atlas of Canada, retrieved from Natural Resources Canada (2019) through the Open Government License. Base map in (*b*) was modified from Vincent et al. (2011). Maps were created using ArcMap 10.6.1.

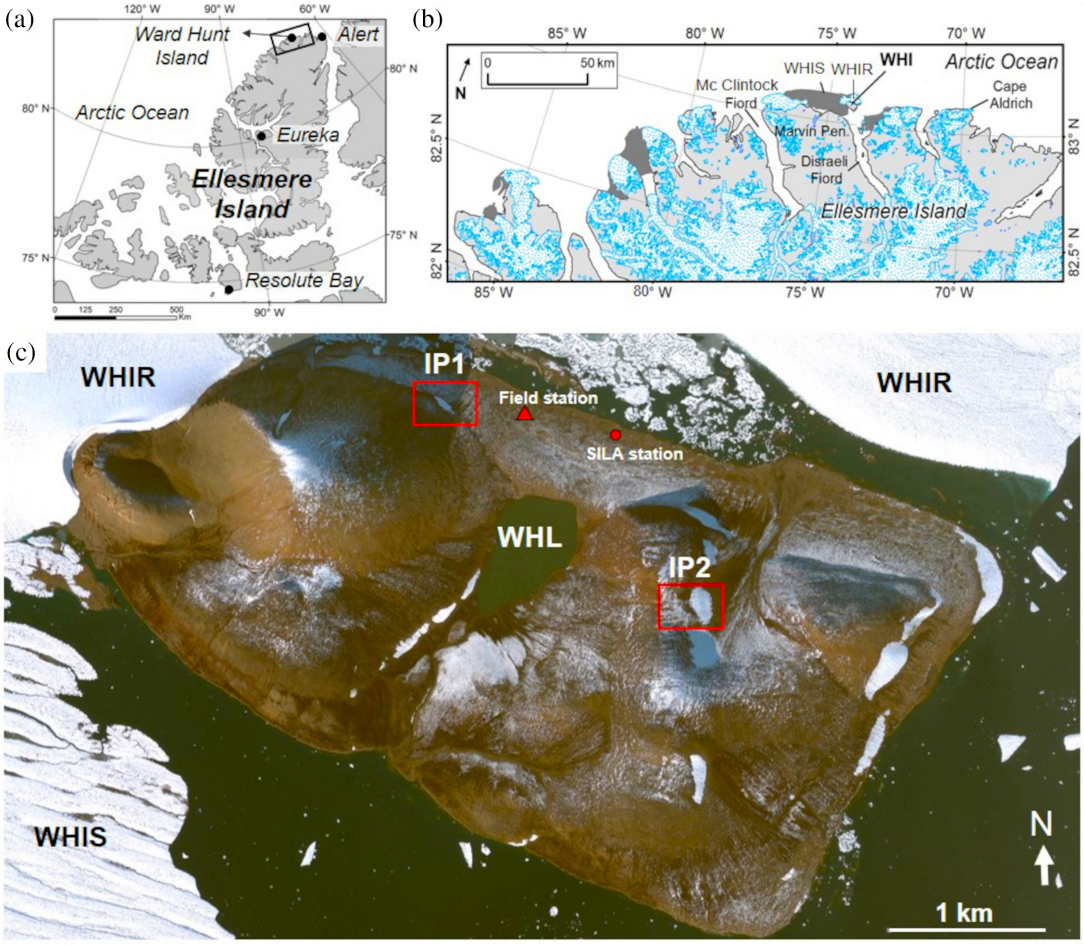

26 August 2011 during a period of substantial warming. They were chosen for their different topographic settings (i.e., elevation, orientation, and position on the slope), their different morphology, their large size, and their accessibility from the research station (Fig. 1*c*).

Seasonal snowpack characterization

Snowpits were dug on both ice patches in early June 2017 (Sp1_17a and Sp2_17) before any melting event had occurred (Fig. 2). On IP1, the snowpit Sp1_17a was compared with another one made in early June 2016 (Sp1_16) at the same location to study the interannual variability of the snow properties. At IP1, an additional snowpit was dug in early July 2017 (Sp1_17b), three weeks after the beginning of the melt season. This pit, made 4 m away from Sp1_17a, was used to document the structure of the snowpack in an advanced melting stage

Fig. 2. Oblique photograph taken from helicopter showing the ice patches selected for this study: IP1 (transverse ice patch) and IP2 (circular ice patch). The snow analysis and ice coring were undertaken in summers 2016 and 2017. The extent of the ice patches at the end of the particularly warm summer 2011 was inferred from the GEOEYE image shown in Fig. 1. Details of snowpits, ice cores, and ice samples are presented in Supplementary Table S1[2].

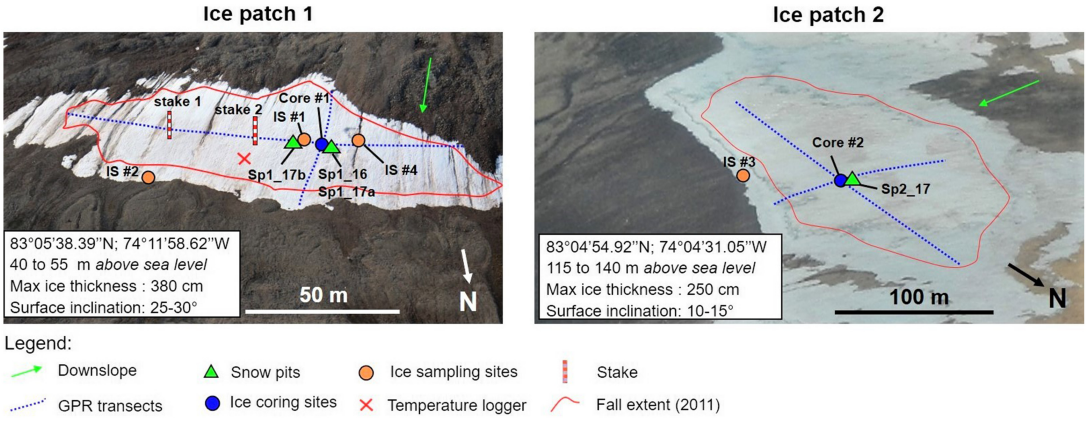

and to understand the evolution of the snow properties and the formation of basal ice throughout the melt season. To estimate ice growth at the base of the snowpack, two graduated stakes were inserted vertically into the snowpack down to the ice surface on IP1 in early June 2017 (Fig. 2). The level reached by the newly formed superimposed ice was then read on 8 July. Data on the snowpits and the snow analysis procedure are detailed in Supplementary material (Supplementary Table S1[2]) and Appendix A.

To interpret the snow metamorphic processes that occurred throughout the cold season, the bulk temperature gradient in the snowpack and wind speed were measured for IP1. We relied on measurements of the air and ice surface temperature throughout the cold season 2016/17 to estimate the temperature gradient through the snowpack. The air temperature was recorded at hourly intervals by a sheltered sensor U22-001 (Hobo®; resolution of 0.02 °C, uncertainty of ± 0.21 °C) set at 1 m above the soil surface and installed 30 m off the front of the ice patch. The ice surface temperature was recorded at hourly intervals by a data logger Trix-8 (LogTag®; resolution 0.1 °C, uncertainty of ± 0.5 °C) installed 15 cm above the ice surface on a wooden pole frozen in the ice, 4 m above the frontal edge of IP1. The height of snow measured above the sensor was 205 cm in early June 2017. The average temperature gradient (ΔT in K m^{-1}) was calculated using eq. (1):

$$\Delta T = (T_{is} - T_{ss})/h \quad (1)$$

where h is the snowpack height, T_{is} is the temperature at the snow/ice interface, T_{ss} is the temperature at the snow surface and is assumed to be equal to the air temperature, except when the latter is above 0 °C in which case T_{ss} is assumed to be equal to 0 °C. As T_{ss} in the dark or under low insolation was equal to or less than the air temperature and given that the U22-001 sensor was on a north-facing slope that received little insolation, the gradient calculated here is, therefore, a lower limit of the actual gradient. The height of snow through the cold season 2016/17 was inferred from the data provided by a Sonic SR50 (Campbell Scientific; resolution 0.25 mm; uncertainty ± 1 cm) installed at the SILA weather station located 1 km west of IP1 (Fig. 1c). The snow gauge is installed on a seasonal snow

[2]Supplementary data are available with the article at https://doi.org/10.1139/as-2021-0011.

patch and provides reliable data to understand the snow dynamics in a preferential accumulation site. The raw data has then been adjusted using a correction coefficient (×1.5) to make the end of winter snow height recorded at SILA consistent with the snow height measured in the central part of IP1 in June 2017.

Ice sampling procedure

The microstructural study of the ice was based on the analysis of ice cored in both patches (see Supplementary Table S1[2] for detailed information). A complete sequence of the ice body, from the top layers to the bottom, was retrieved from IP1 (core #1) and IP2 (core #2) (Fig. 2) during the 2017 field season. The coring procedure is detailed in Appendix B. For both sites, the coring location was selected according to ground penetrating radar surveys that allowed identification of where the ice was deepest. Additional ice samples were collected from IP1 and IP2 for comparison (Fig. 2, Supplementary Table S1[2]). Seasonal basal ice samples were collected at the bottom of the snowpit Sp1_17b (IS#1) and at the frontal margin (seasonal fringe) of IP1 (IS#2) and IP2 (IS#3) where the basal ice was newly exposed. Ice samples were also extracted from the sides of a supra-ice channel that drained the meltwater on IP1 (IS#4) (Fig. 2). The aim was to understand the properties of the newly formed ice to infer the transformation processes of snow to ice and to document the consequence of water inputs to the ice transformation and recrystallization processes. All ice cores and samples were described, measured, and photographed in the field. They were then sealed in plastic bags and kept frozen in a cold room at –12 °C.

The crystalline structure of the ice

A total of 120 thin sections were made for this study. The thin section preparation, detailed in Appendix C, followed the procedure reported by Langway (1958) and Østrem (1963). The post-processing step consisted of automatically detecting the crystal boundaries using the open-source imaging software ImageJ® (Fig. 3). The high resolution of the photography allows the detection of crystals as small as 0.2 mm. A computation of the 2D morphometric properties of each ice crystal detected in a thin section was performed using ImageJ (Analyze particle function) to measure the crystal size, defined by the surface area (A, in mm^2) the major axis length (L, in mm) and the crystal shape obtained by computing the roundness parameter (R) (Appendix C). We used the following crystal size classes derived from Ragle et al. (1964): very fine, <5 mm^2; fine, 5–10 mm^2; medium, 10–50 mm^2; coarse, 50–100 mm^2; and very coarse, >100 mm^2. Finally, the 2D shape and organization of the crystals were studied using shape anisotropy (Gay and Weiss 1999), which describes the elongation of the crystals in a preferential direction. It was calculated by the ratio between the length of the crystal measured in the horizontal (Lx, in mm) and vertical (Lz, in mm) planes (Supplementary Fig. S1[2]). C-axis orientations were not determined. The major limitation with the thin section is the impossibility of accurately measuring a 3D structure with a 2D perspective. The planar thin section randomly cuts ice crystals and their apparent shape and size do not necessarily reflect the true values. Some methods have been proposed to correct this bias (e.g., Gow 1969; Alley and Woods 1996), but the most common and accepted practice in the literature is to present uncorrected results (Thorsteinsson et al. 1995; Coulombe et al. 2019).

Gas and sediment inclusions in the ice

To complement ice crystallography, a description of the inclusions of air and sediment (shapes, sizes, concentrations, and distributions) trapped in the ice gives insights in ice forming conditions. The characterization of the air and sediment inclusions in both ice cores was done with high-resolution (0.195 × 0.195 × 0.4 mm voxel volume) 3D X-ray computed tomography scans (CT-scans) provided by a Siemens Somatom 64 scanner at

Fig. 3. Investigation of the ice properties through (*a*) ice crystal analysis using thin sections and (*b*) gas and sediment inclusion analysis using microtomodensitometry (CT-scan).

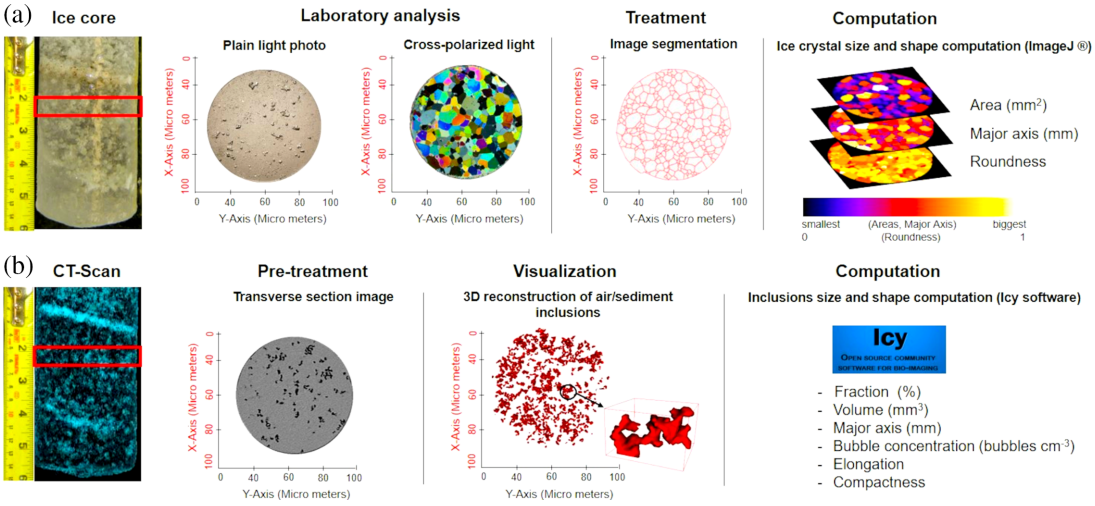

the Institut National de la Recherche Scientifique (INRS-ETE) in Québec City, Québec, Canada (Appendix D, CT-scan images are available in open-access files, see "Data availability statement", Fortier and Davesne 2021*a*). Processing of the DICOM images was performed using the ImageJ software® following the procedure of Crabeck et al. (2016). From the stack of images, a high-resolution sub-millimetre profile of the porosity (i.e., air fraction) was extracted. Air fraction was expressed by the porosity (ϕ in %) for a given volume of ice (V) and was then converted into bulk density (ρ_i in kg m^{-3}) of the ice (Appendix D; Supplementary Fig. S2[2]). For the ice samples IS#1 to #4 for which no CT-scan images were obtained, the bulk density was obtained in the laboratory by cutting a disk 5 cm thick from the core for which mass was measured with an electronic balance (resolution: 0.001 g). When a sample had an irregular shape, its gross volume was determined by submerging samples sealed in plastic bags into 2 L of cold water in a 20 cm diameter graduated cylinder and by measuring the water displacement (Kawamura 1990).

The bubble number density (bubbles cm^{-3}), and the size and morphology of air bubbles were computed from the three-dimensional CT images using the Icy imagery software package (De Chaumont et al. 2012, Legland et al. 2016). The software allowed detecting each bubble larger than the voxel resolution (0.0152 mm^3) and to reconstruct their surface by triangular meshing. The 3D visualization of air bubbles in the ice, coupled with naked-eye observation of the thin sections, was used to detect and count the fracture density in the ice cores (Supplementary Fig. S3[2]). In addition, a 3D morphological analysis of the air bubbles was performed using the plugin 3D-analysis that allowed to compute the long-axis (L, in mm), the volume (V, in mm^3), the compactness (C), and the elongation index (El) of each mesh (Fig. 3). According to their volume, the air bubbles derived from the CT scans were classified into 3 categories: micro-bubbles (V < 1 mm^3), large bubbles (1 < V < 10 mm^3) and macro bubbles (V > 10 mm^3) (Crabeck et al. 2016). The C is the normalized ratio between the surface areas and the volume of a bubble and is related to the shape and the roundness of bubbles (Zhao and Wang 2016). Values tend to 1 for a sphere, whereas it tends to 0 for a highly irregular shape. The EI is the ratio between the largest radius and middle radius of the bubbles. The elongation value is close to 1 for rounded bubbles and increases for those that are elongated. From those shape descriptors, air bubbles were

divided into four classes, namely elongated cylindrical bubbles (ECb) ($C > 0.15$; $El > 2$), sub-spherical bubbles (SSb) ($0.15 < C < 0.4$; $El < 2$), spherical bubbles (Sb) ($C > 0{,}4$; $El < 2$) and irregular bubbles (Irb) ($C < 0.15$; $El < 2$).

The concentration of sediments (kg m^{-3}) was measured in the laboratory by cutting slices of ice cores, calculating their volume, and melting them in individual pre-weighed aluminum containers. The samples were then dried in an oven and weighed with a high accuracy scale (resolution: 0.001 g). The measurements of sediment concentration were only made in the core sections where sediments were visible to the naked eye. Finally, we collected a sample of material that was a mixture of two distinct bands of sediments between 212 and 218 cm deep in core #2 (IP2) for radiocarbon dating. The sample contained organic debris, including well-preserved fragments of moss, branches, flowers, and leaves (Supplementary Fig. S4[2]). The sample was pretreated (HCl, NaOH, HCl) at the Radiocarbon Dating Laboratory (Université Laval, Québec, Québec, Canada) and ^{14}C dated by accelerator mass spectrometry (AMS) at Keck Carbon Cycle AMS Facility (University of California, Irvine, California, USA). The radiocarbon date was calibrated with the CALIB 8.2 online program (Stuiver et al. 2021) using the IntCal13 calibration data set (Reimer et al. 2013)

Environmental monitoring

To infer the formation processes of the ice, we also relied on a set of environmental data monitored at IP1 including time lapse photographs, ice temperature, and meltwater outflow discharge. The time-lapse photographs were taken by an automatic camera (Spypoint® Force-11D) installed in front of IP1 since July 2016 (Fortier and Davesne 2021*b*). The ice temperature data were measured between July 2017 and July 2019 by a chain of thermistors (resolution ± 0.001 °C; uncertainty ± 0.1 °C) at depths of 0, 50, 100, 150, 200, 250, 300, and 320 cm installed in the drill hole of Core #1 on IP1 (Fortier and Davesne 2021*b*). A white perforated PVC pipe was placed into the borehole in which the cable was inserted. Water was then poured in and around the pipe to set it and guarantee optimal thermal contact with the ice body. The deepest thermistor, at 320 cm, was in contact with the bedrock. Thermistors were connected to a multichannel data logger (Systems Smart Reader Plus 8™, ACR Systems Inc., Surrey, BC, Canada), which recorded temperatures at an hourly interval.

Results

Seasonal snow accumulation over the ice patches

The snowpack properties and vertical structure of the pits Sp1_17a, Sp2_17, Sp1_16, and Sp1_17b are shown in Fig. 4. In early June 2017, the snowpack stratigraphy shows the same structure on IP1 (Sp1_17a) and IP2 (Sp2_17). The upper section consisted of hard wind slabs with density values exceeding 400 kg m^{-3} (Fig. 4*a*, *b*). These slabs were topped by a surface layer of fresh snow made of fragmented snow crystals. In both snowpits, the proportion of faceted grains gradually increased with depth. Below a certain height (160 cm in Sp1_17a and 80 cm in Sp2_17), the wind slabs exhibited an early stage of recrystallization. The grain size was slightly larger than in the upper sections. The bottom-most layer was a thin layer of depth hoar (less than 10 cm thick) with crystal size not exceeding 2–4 mm near the contact with the ice substratum. In both cases, the first few centimetres of the ice surface consisted of weathered ice with loose coarse crystals of ≈5 mm in size. Specifically for the snowpit Sp2_17, a layer (≈15–20 cm) of sediment and very hard-packed snow (ρ_s = 580 kg m^{-3}) was found just above the depth hoar (Fig. 4*b* and Supplementary Fig. S5[2]). The sediment content of this snow layer reached 10.9 ± 0.97 kg m^{-3}. The snowpit Sp1_16 dug in early June 2016 (Fig. 4*c*) showed properties similar to Sp1_17a made one year

Fig. 4. Graphical representation of the stratigraphy and physical properties of the seasonal snowpack measured over perennial ice patches. (*a* and *b*) Snowpits Sp1_17a and Sp2_17 were dug on IP1 and IP2, respectively, in early June 2017, (*c*) the snowpit Sp1_16 was dug one year earlier (7 June 2016) at the same site as Sp1_17a, and (*d*) the snowpit Sp1_17a was dug on 2 July 2017 close to the site of Sp1_17a. Snow-type symbols are those used by Fierz et al. (2009) and Domine et al. (2018). The horizontal grey lines represent the stratigraphic discontinuities that delimit the different layers observed in the snowpack. The thickness of new basal ice could not be estimated from the Sp1_17b snowpit as the lower boundary with the previous year's ice was unclear. The total thickness of basal ice in summer 2017 was obtained from stake readings.

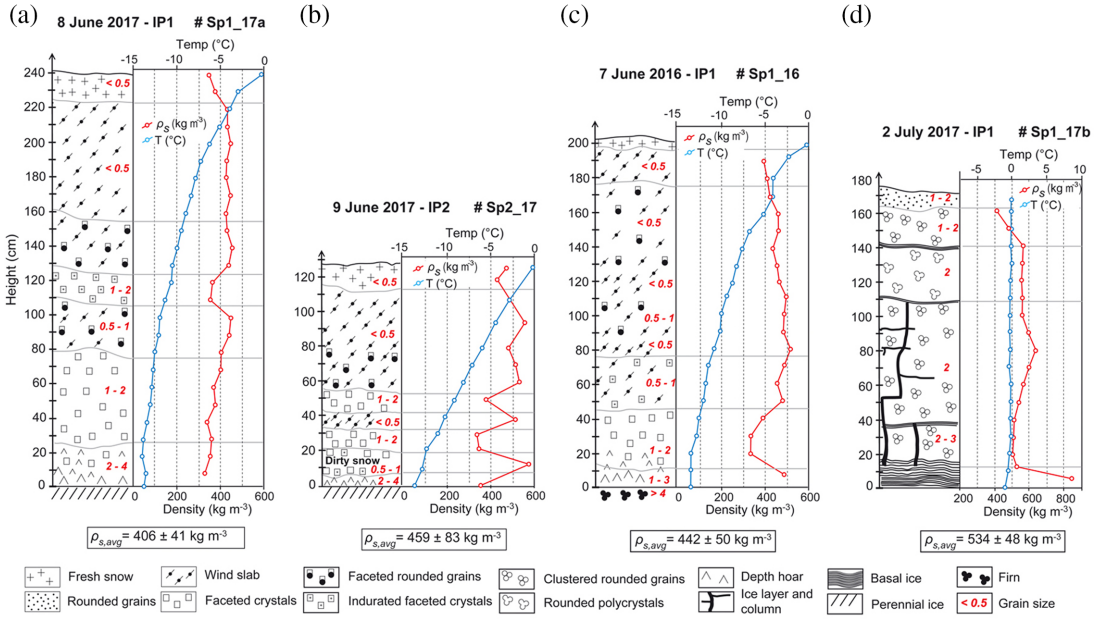

later at the same location, with the difference that in 2016 the basal depth hoar layer was lying on a surface of granular and compact old snow identified as firn.

On 2 July 2017, the snowpack at the snowpit Sp1_17b was 175 cm deep including a ~15 cm deep surface layer of fresh snow added by a storm on 29–30 June 2017 (Fig. 4*d*). At that time, the entire profile was isothermal and consisted of unsaturated wet snow consisting of clustered rounded grains, and snow density reached values up to 640 kg m^{-3}. Within the snowpack, discontinuous horizontal ice layers, up to 3 cm thick, and large vertical percolation channels made of solid ice up to 6 cm in width were present (Supplementary Fig. S6[2]). The lowest part of the snowpit consisted of a basal ice layer overlaid by a water-saturated layer of coarse granular snow. All the percolation channels reached the basal ice layer. On 8 July 2017, the reading of the stakes installed in IP1 gave a new ice layer of 27 cm and 34 cm upon the former ice surface for stakes 1 and 2, respectively. The density of the samples of basal ice collected at the base of Sp1_17b was 876 ± 19 kg m^{-3} (n = 5), on average (Table 1, sample IS#1), and the overall density of the snowpack, excluding the basal ice and internal ice structures, was 534 ± 48 kg m^{-3}.

The bulk temperature gradient values in the snowpack on IP1 through the cold season 2016/17 is shown in Fig. 5. Three main periods can be identified. Period 1 is short and consists of the early cold season when a large temperature gradient (>100 K m^{-1}) developed into the shallow snowpack (5 to 15 cm deep). Period 2 started when the snowpack became deep enough to drastically reduce the bulk temperature gradient (<20 K m^{-1}). These low gradient conditions extended during most of the cold season and the gradients then

Table 1. Mean (± SD) of major axis, crystal surface area, roundness (inverse of the aspect ratio), and density of the upper and lower section of IP1 and IP2. In addition, same data were obtained for the ice samples collected at the bottom of the seasonal snowpack on IP1 (IS#1), on the freshly exposed ice near the frontal margin on IP1 (IS#2) and IP2 (IS#3), and on the side of a supra-ice channel on IP1 (IS#4). Values in parentheses are the number of samples for which the hydrostatic density was measured. See Supplementary Fig. S8[2] for examples of photographs of thin sections of ice samples. X means the horizontal plane, and Z means the vertical plane of the ice cores.

			Major axis (mm)	Surface area (mm^2)	Roundness (Index)	Density ($kg\ m^{-3}$)
Ice cores						
Upper section	IP1	X	1.55 ± 1.05	2.35 ± 1.78	0.70 ± 0.01	895 ± 19
		Z	1.51 ± 0.92	1.88 ± 0.79	0.69 ± 0.01	
	IP2	X	1.80 ± 0.54	2.23 ± 3.94	0.70 ± 0.02	884 ± 26
		Z	1.51 ± 0.26	2.04 ± 2.99	0.69 ± 0.02	
Lower section	IP1	X	7.69 ± 2.29	43.42 ± 25.69	0.63 ± 0.03	914 ± 3
		Z	6.22 ± 1.92	36.13 ± 20.67	0.64 ± 0.02	
	IP2	X	6.03 ± 1.86	28.83 ± 11.40	0.67 ± 0.01	901 ± 43
		Z	7.11 ± 1.44	30.39 ± 9.95	0.65 ± 0.02	
Ice samples						
Basal ice	IS#1		2.67 ± 0.29	4.91 ± 1.21	0.73 ± 0.02	876 ± 19 (n = 5)
	IS#2		2.17 ± 0.13	3.15 ± 0.50	0.73 ± 0.01	862 ± 12 (n = 3)
	IS#3		1.58 ± 0.34	1.66 ± 0.66	0.75 ± 0.01	865 ± 14 (n = 3)
Channel ice	IS#4		10.48 ± 3.51	68.80 ± 55.44	0.47 ± 0.05	909 ± 03 (n = 4)

approached 0 K m^{-1} when the snowpack started to warm up in April. From May, the air temperature became warmer than the temperature at the snow–ice interface, so that the temperature gradient has turned slightly negative; this is Period 3. At the end of the cold season, almost all of the snowpack was at 0 °C on 23 June except the very basal layer. The temperature gradient was, therefore, zero above that layer.

Perennial ice properties

General ice structure of ice cores

The visual examination of the overall ice cores IP1 and IP2 (Fig. 6) shows an abrupt change in the physical parameters of the ice at a depth of 130 cm. In the upper section, the vertical variation in ice porosity creates an interplay of milky ice and clear translucent ice facies. Some brownish-red-shaded, more or less opaque layers are also present at various intervals due to dust and coarser sediment inclusions. Various ice facies and the sediment layers formed a series of bands with the same inclination and orientation. They dip downward with an angle of 20° to 25° for IP1 and 13° to 18° for IP2, which follow the ground surface slope angle (Fig. 2). The lower sections present a higher proportion of clear ice and are marked by larger sediment inclusions than in the upper sections. The oblique banded pattern is less evident and absent in some parts. The lower sections are marked by a high frequency of micro-fractures that randomly cut across the cores (Fig. 6).

Crystal size and shape

The upper section of both ice cores #1 and #2 exhibited similar ice petrography. The thin section analysis revealed a pattern consisting of randomly arranged very fine polygonal crystals (Fig. 6 and Supplementary Fig. S7[2], Table 1). The crystal size distribution is narrow (low variance) and is nearly constant along the vertical profile. The comparison between the measurements obtained from horizontal (X plane) and vertical (Z plane) thin sections

Fig. 5. Evolution of the daily air and ice surface temperature, of the daily snow depth (inferred from the SILA station), and of the temperature gradient in the snowpack on IP1 through the cold season 2016/17 calculated from eq. (1). Vertical dashed lines delimit the three periods in the temperature gradient evolution. "Sp" during period 3 shows when snow pits were dug.

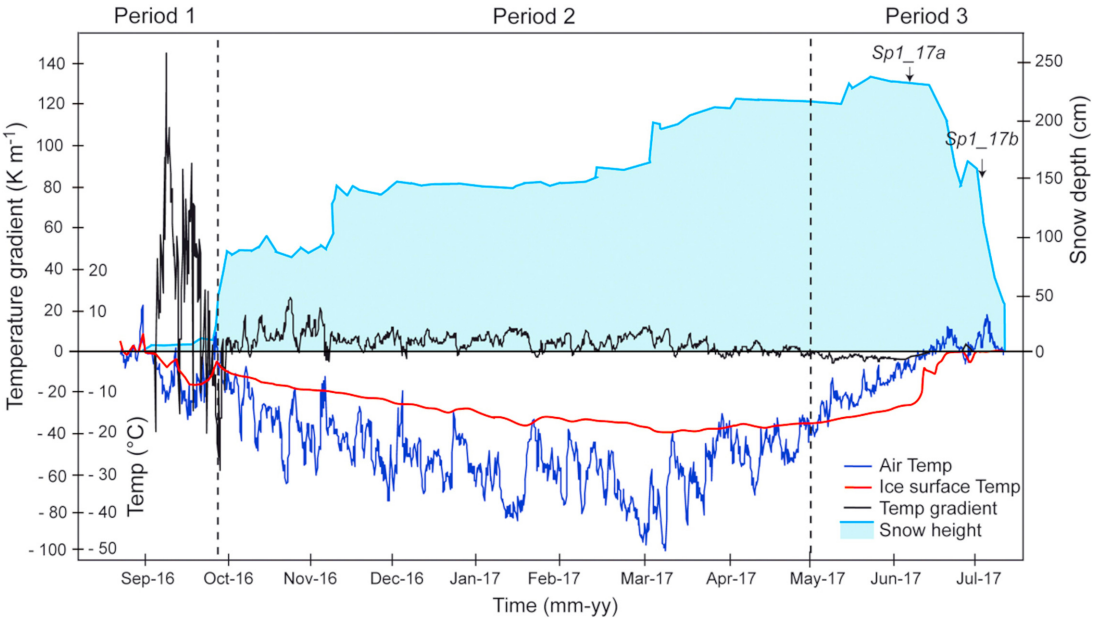

shows an anisotropy ratio close to 1 along the upper sections, indicating no preferential elongation of the crystals. This equiaxial character of ice crystals is also revealed by the similar high roundness values (R) for both X and Z planes. Under cross-polarized light, the thin sections revealed a wide range of crystals interference colours (Fig. 6), indicating that they have a randomly oriented c-axis. In the lower sections of the ice cores #1 and #2, the crystal size is significantly higher, ranging from medium to coarse sizes (Fig. 6 and Supplementary Fig. S7[2], Table 1). The variance in the crystal size is higher and the vertical variability is much more pronounced than in the upper sections. Very coarse crystals exceeding 100 mm^2 are found in the sections where the ice is the most translucent. Coarser crystals are up to 500 mm^2 in core #1 and 230 mm^2 in core #2. The ice crystals have a more irregular shape and a slight vertical elongation as suggested by the lower R values and the shape anisotropy ratio values below 1.

The crystallography of additional ice samples is presented in Table 1 and Supplementary Fig. S8[2]. The basal ice collected at the bottom of the snowpit Sp1_17b (IS#1) and in the frontal edge of IP1 (IS#2) and IP2 (IS#3) consists of very fine rounded grains. The ice samples collected on the sides of a supra-ice channel (IS#4) are characterized by very coarse ice crystals. Larger crystals had a major axis up to 50 mm and were mostly elongated (R = 0.47 ± 0.05).

Gas inclusions and density of the ice

In the upper sections of both ice cores #1 and #2, air inclusions are characterized by high variability of sizes, concentrations and shapes (Fig. 6 and Supplementary Fig. S9[2]). Large ($1 < V < 10$ mm^3) and macro-bubbles ($V > 10$ mm^3) account together for 49% and 47% of the bubble population, respectively (Fig. 7). The larger bubbles are well dispersed in the ice and they are occasionally concentrated into thin oblique layers, which form high porosity bands (Supplementary Fig. S9[2]). The general bubble concentration is low, especially in

Fig. 6. Physical description of the ice cores retrieved at the (*a*) IP1 and (*b*) IP2 sites. A is the crystal surface area, D1 and D9 are 10th percentile and the 90th percentile, respectively; Lx and Lz are the maximum length of the ice crystals for the horizontal plane (X-plane) and vertical plane (Z-plane), respectively; ρ_i is the ice density, V and C are the bubble volume and bubble concentration, respectively.

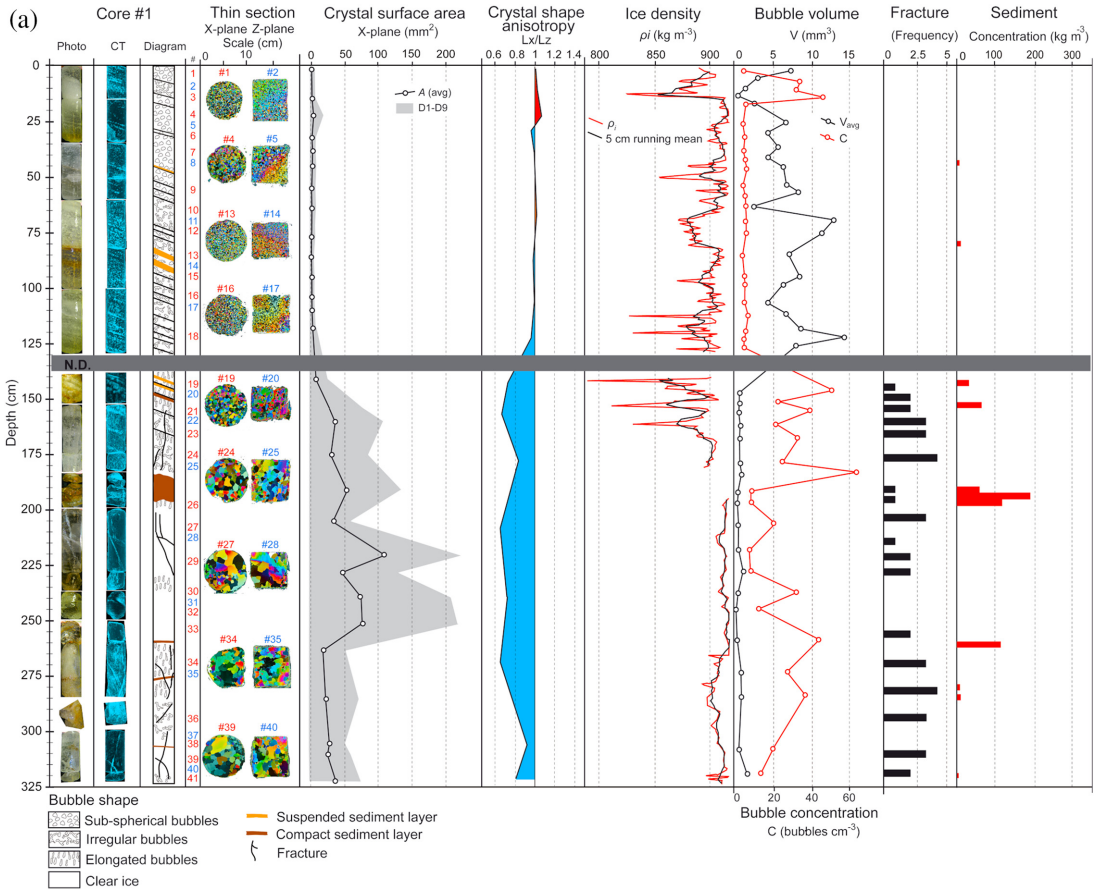

core #1. Examination of the morphology of the air inclusions showed a high occurrence of irregular shapes in the large and macro-bubble population, whereas sub-spherical shapes dominate the micro-bubbles ($V < 1$ mm^3) (Figs. 6, 7, and Supplementary Fig. S9[2]). In the lower section of cores, the micro-bubbles predominate with 85% and 75% of the bubble population for IP1 and IP2, whereas macro-bubbles are mostly absent (<0.5% in both cases); the average bubble number density is higher (Fig. 7). The micro-bubbles are heterogeneously dispersed through the ice, so that no well-developed banded structure exists. The larger bubbles are mainly concentrated in fractures, forming trains of sub-spherical to elongated bubbles (Supplementary Figs. S3[2] and S9[2]). The small and large bubbles are generally elongated along the Z plane, whereas the micro-bubbles are roughly spherical (Supplementary Fig. S9[2]). Translucent ice was typically associated with coarser ice crystals (Fig. 6).

The high proportion of large and macro-bubbles in the upper sections of cores #1 and #2 led to a higher ice porosity (Fig. 7), explaining density values around 890 kg m^{-3}. The density profiles revealed pronounced micro-scale variations. The ice with lower density (<850 kg m^{-3}, Fig. 6) was generally in the layer with a high proportion of macro-bubbles. By contrast, the lower section of core #1 is marked by a very low porosity, given a high

Fig. 6. *(Concluded).*

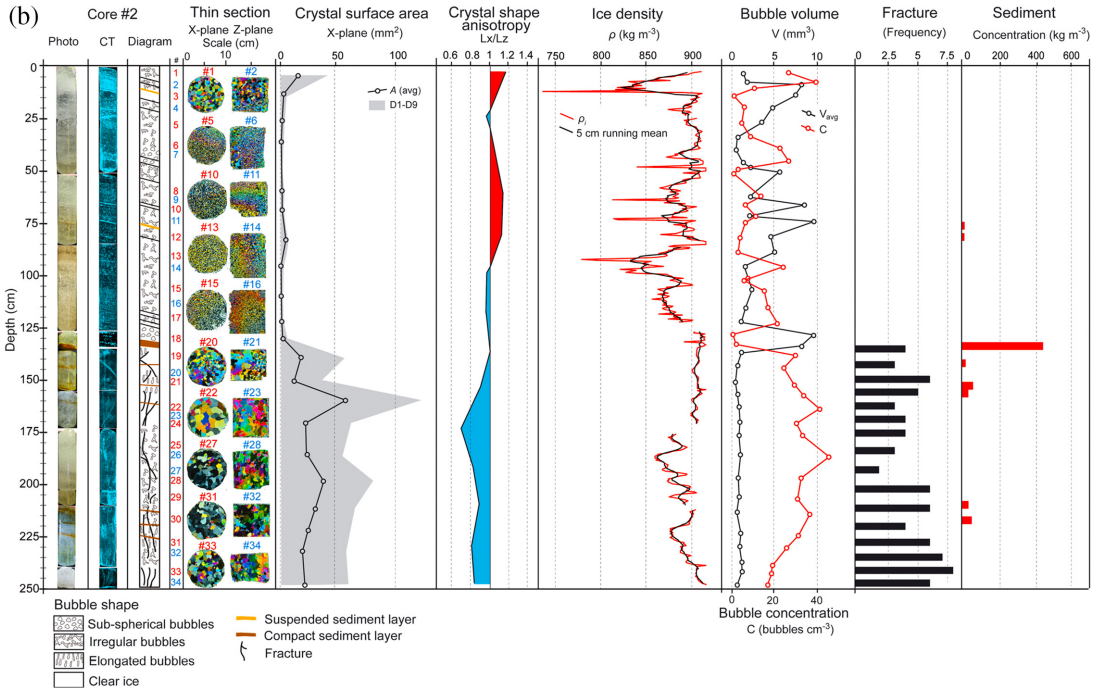

density of 914 ± 3 kg m^{-3} on average. Sections of translucent ice are very close to the pure ice value. For core #2, the density is lower with an average value of 901 ± 4 kg m^{-3}, due to a higher porosity (Figs. 6 and 7). The density of the ice samples IS#1 to IS#4 is presented in Table 1.

Sediment content

Both ice cores #1 and #2 contained sediment inclusions. In the upper sections, the presence of sediment occurred as oblique bands of suspended silty sediment in the ice (Figs. 6 and 8*a*). Their concentrations were very low (>10 kg m^{-3}) and their composition mainly consisted of mineral particles, derived from local limestone and volcanic rock (Trettin 1991), in which sparse organic fragments were observed. By contrast, the lower sections of ice cores are marked by several compact bands of material. The sediment deposits most often consisted of thin sheets of silty to sandy particles, sometimes mixed with organic fragments (Fig. 8*b*) and occasionally formed layers up to several centimetres thick (Fig. 8*c*). The larger sediment inclusion was found in core #1 at 190 cm depth. This consisted of a 15 cm thick layer of poorly sorted angular rock fragments and sand mixture bonded by ice (Fig. 8*d*). The hiatus in the sequence of core #1 between 130 and 140 cm corresponded to a layer of fine-grained sediment that was lost during the coring operation. As shown in Fig. 8*e*, samples of newly formed ice collected in the seasonal fringe of IP1 (IS#2, 0–20 cm) contained fine-grained sediments suspended in the ice as suggested by the brown-red coloration of the ice. In the samples collected in the supra-ice channel on IP1, a mixture of coarse gravel and sand is embedded in the ice (Fig. 8*f*). AMS radiocarbon dating of organic fragments found in a sediment layer embedded in the ice at 212–218 cm depth in IP2 gave an age range of 3453–3561 cal BP (2-sigma) with a median value of 3487 ± 20 cal BP.

Fig. 7. Summary of the ice porosity, and the bubble size distribution, bubble volume and bubble concentration in the upper and lower sections of IP1 and IP2. V is the bubble volume. The red line in the box plot is the median, the black cross is the mean and the circles represent the outliers.

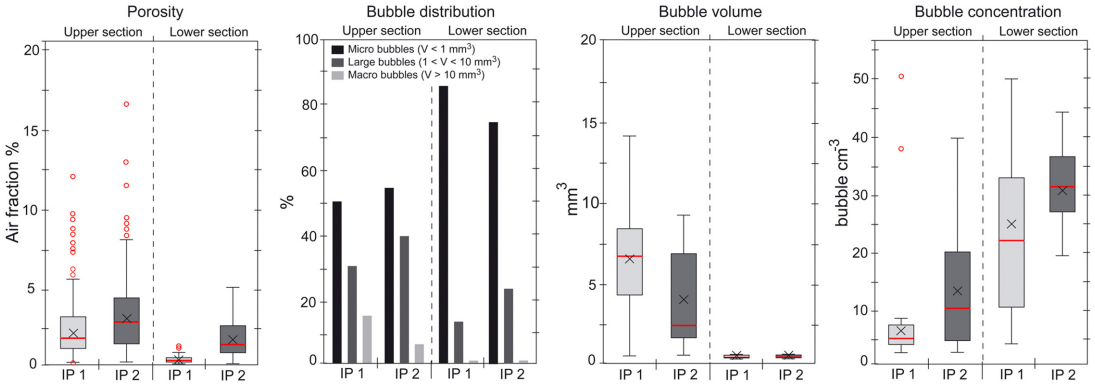

Thermal regime of the ice patch and snow conditions

The mean annual ice temperature averaged over the two years of records (July 2017 to June 2019) gives a value from −13.2 °C at the ice surface to −11.1 °C at the ice–bedrock contact (Fig. 9*a*). The ice surface and subsurface (−50 cm) showed a contrasting thermal regime between the two years, reflecting interannual variabilities in the snowpack regime and the severity of summer ablation. The time-lapse photograph presented in Fig. 10*a* shows that the surface of the ice patch experienced an advanced stage of melting in late summer 2017 as most of its surface was exposed ice. The following fall, the onset of a deep snowpack was late as the snow depth did not exceed 100 cm until 29 October (Fig. 9*c*). Consequently, the ice surface cooled rapidly with the temperature dropping to −27 °C on 19 October (Fig. 9*b*). In contrast, in summer 2018, the ice surface from the previous summer remained buried under the seasonal snowpack throughout the summer (Fig. 10*b*). In addition, significant precipitation on 24 August brought a high amount of fresh snow early in the season (Fig. 9*c*). This thick snowpack reduced the cooling of the ice body at the beginning of the cold season. These contrasting surface conditions, however, did not have a significant effect at depth. At the contact between the ice body and the bedrock, the temperature fluctuated from about −6 °C during the first half of September to about −15 °C in mid-June for the two years (Fig. 9*a*, *b*). All depths experienced an abrupt rise in temperature in June. The highest temperature change occurred at the surface and subsurface (−50 cm) where the daily temperature increased by nearly 15 °C within a few days to reach the melting point (Fig. 9*b*).

Discussion

Snow stratigraphy and metamorphism over the ice patches

The typical polar desert snowpack is shallow and generally <30 cm deep (Domine et al. 2018; Royer et al. 2021). The physical properties of this snow, such as density and microstructure, evolve throughout the cold season according to metamorphic processes driven by meteorological conditions—mostly wind, air temperature, and cloudiness—as well as water vapor gradient within the snow (Colbeck 1982). In polar deserts, the period of strong vertical temperature gradient (>20 K m^{-1}) is typically short as the soil temperature drops quickly in the early winter because of the lack of soil moisture (Domine et al. 2018). As a result, the depth hoar layer that forms at the bottom of the seasonal snowpack is shallow, ranging from 25% to 30% of the snow column, although significant local variations may

Fig. 8. Examples of the various forms of sediment inclusions found in the ice. (*a*) A band of suspended sediments at 45 cm depth in the upper section of IP1; (*b*) a thin layer of fine-grained sediments at 145 cm (lower section) depth in IP2; (*c*) a 2 cm thick band of compact fine-grained sediments at 135 cm depth (lower section) in IP2; (*d*) a 15 cm thick band of ice-bonded gravel and sand at 190 cm depth in IP1; (*e*) brown coloration of ice sample IS#2 collected in the seasonal fringe of IP1 due to suspended very fine sediments; (*f*) mix of gravels and fine-grained sediments frozen in the side of a supra-ice channel on IP1.

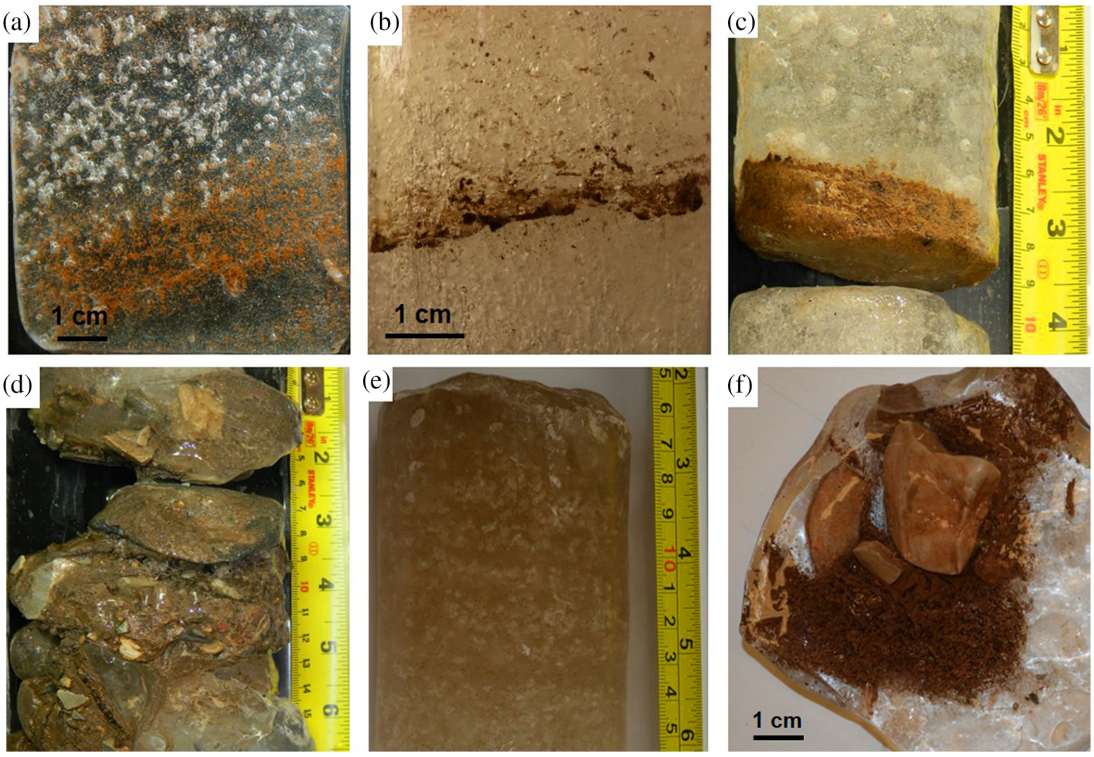

occur depending on the spatial variability of soil moisture and microtopography (Domine et al. 2018; Davesne et al. 2021; Royer et al. 2021). Later in the season, the temperature gradient decreases as the snowpack thickens and the temperature of the frozen soil drops (Domine et al. 2018). In those conditions, the wind slabs that form in polar deserts cannot be transformed into indurated depth hoar, so that the top layers of the snowpack consist of small, rounded grains showing little, if any, signs of recrystallization and growth (Royer et al. 2021).

In the case of ice patches, seasonal snow evolved under markedly different conditions (Fig. 4). Our observations suggest that the end of winter physical properties of snow observed on the ice patches were mainly due to wind-driven processes that determined the initial snow structure and by the deep snow accumulation that led to snow compaction. As indicated by Fig. 5, the strong temperature gradient (>20 °C m^{-1}) was short-lived, just 3 weeks in fall 2016 (Period 1). This only allowed the transformation of the very basal layer into depth hoar (Fig. 4), the fraction of which was typically less than 5% of the snow column. Given the high recurrence of strong winds and drifting snow episodes in polar desert environments and the resulting rapid accumulation of snow on the ice patch in fall, we consider that unfavourable conditions for the development of depth hoar to be the rule at WHI

Fig. 9. Thermal regime of the perennial ice patch IP1. (*a*) Mean monthly and annual ice temperature profile averaged over the two years of record (July 2017–June 2019) from the 320 cm deep borehole drilled in IP1 (Fortier and Davesne 2021*b*); (*b*) daily evolution of ice temperature at various thermistor depths and (*c*) daily evolution of the air temperature and snow depth provided by SILA station between July 2017 and June 2019 (CEN 2021). The snow depth data set was corrected by a multiplication coefficient (×1.5) to be representative of the maximal snow depth measured on IP1.

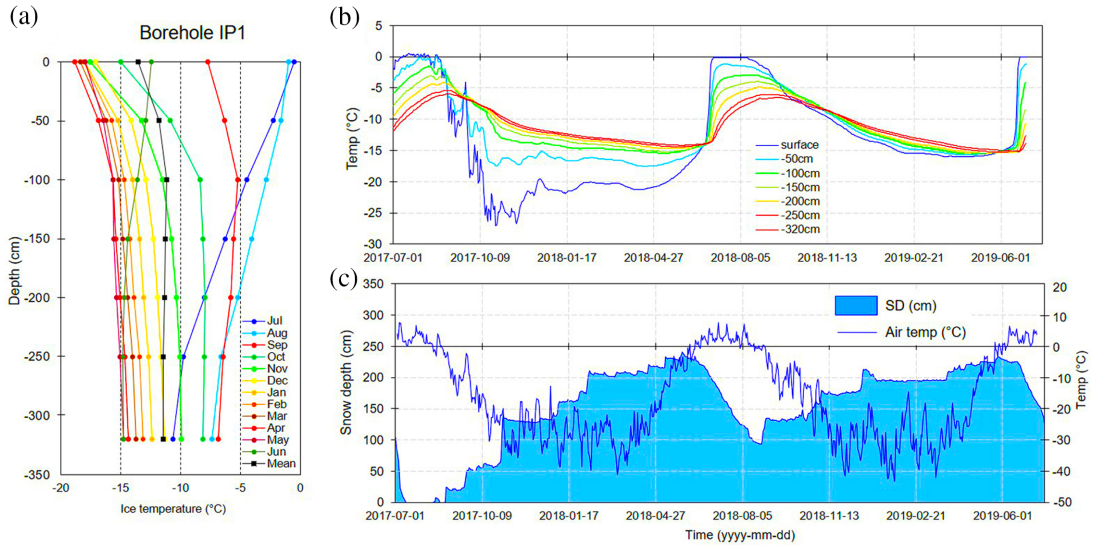

(Domine et al. 2018). In the lower section of the snowpack, the weight of snow accumulation led to further compaction by overburden pressure. This densification increased the thermal conductivity and decreased the permeability of the snow. Both these factors combined to reduce the temperature gradient and water vapor transport, limiting metamorphism to a low grade (Period 2; Fig. 5). In the uppermost layers, we assume that snow also underwent low-temperature-gradient metamorphism (<10 K m^{-1}) during most of the cold season leading to slow sintering of the fragmented crystals (Colbeck 1982; Domine et al. 2008). The resulting snowpack, therefore, had properties distinct from those of a typical Arctic snowpack as depth hoar was confined to a thin layer and the compaction increases snow density to values in excess of most values reported in polar deserts (Domine et al. 2002; Royer et al. 2021) and also in Arctic tundra (Benson and Sturm 1993; Derksen et al. 2009).

In early summer, the onset of the snowmelt period brought rapid changes to the physical and thermal properties of the snowpack. The first stage of snowmelt, known as the warming phase, started with the onset of sustained positive air temperatures, typically during the first half of June (Figs. 5 and 9*b*). At that time, the greater energy input to the snow surface resulted in increased temperature and liquid water content in the topmost layers of the snowpack. Once the snow temperature had reached 0 °C, the melting front then gradually propagated towards the base of the snowpack, initializing rapid wet snow metamorphism that consisted of growth, rounding, and sintering of the snow grains (Colbeck 1982; Pomeroy and Brun 2001). Compaction and high liquid water content of the melting snow increased the snow density to 550 kg m^{-3} (e.g., Sp1_17b; Fig. 4).

As the melting front progressed, the snow became wet and liquid water derived from the melt of the upper snow layers percolated down into the snowpack (flow fingers; Marsh 2006). Over nearly a month (early June to early July) the initial height of snowpack

Fig. 10. Automatic time-lapse photographs of the ice patch IP1. Photo (*a*) was taken in the late summer 2017 (2017-08-06), during which most of the ice patch surface consisted of exposed ice after particularly warm conditions. Photo (*b*) was taken at the end of the cool summer 2018 (2018-08-08) during which a thick seasonal snowpack remained over the ice surface to form a firn layer. The red line delineates the seasonal snow extent from the exposed ice surface.

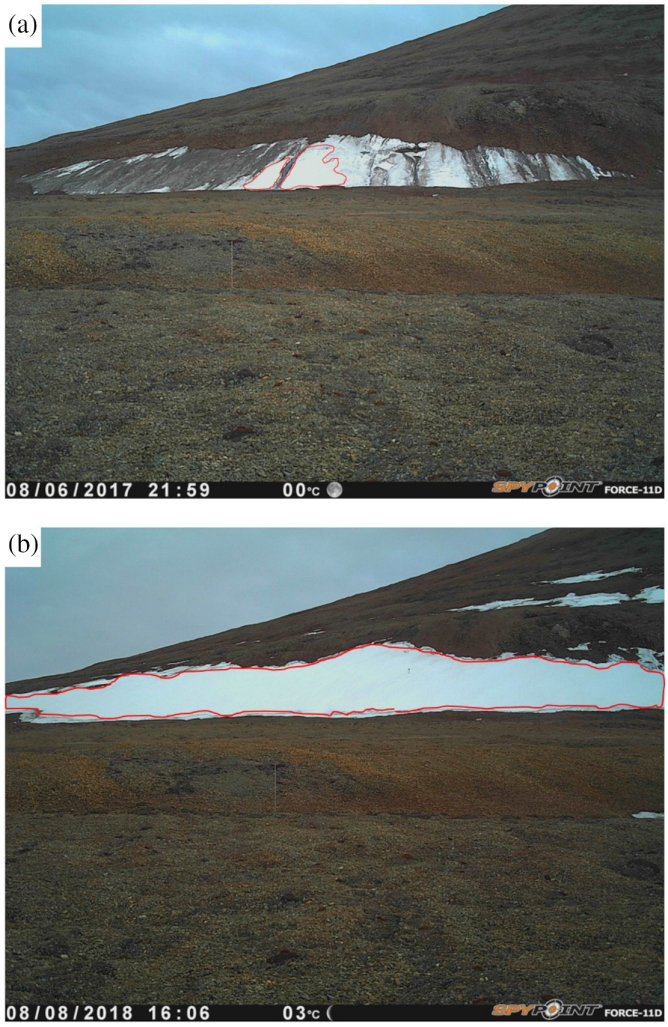

decreased by about 27% (i.e., 70 cm of snow at 500 kg m^{-3} given 35 cm w.e.) (Fig. 4). Much of the percolating meltwater refroze deeper in the snowpack to form ice columns and ice layers (Fig. 4 and Supplementary Fig. S6[2]) (Marsh 2006). When the percolating meltwater reached the cold and impermeable ice substratum, the base of the snowpack became water-saturated and froze, leading to the upward growth of basal ice as superimposed ice, similar to what occurs on Arctic glaciers (Fig. 4) (Woo et al. 1982; Marsh 2006; Obleitner and Lehning 2004).

The refreezing of meltwater into the snow led to the release of latent heat that enhanced snowpack warming as suggested by the rapid temperature increase at the snow–ice interface (Figs. 5 and 9*b*). Once the snowpack was ripe, the snow depth decreased rapidly as almost all the energy input produced snowmelt. At depth, the percolation of the water

enhanced the progressive compaction of the snowpack that led to a density increase as summer progressed.

Structural characteristics and origin of the ice patches

In this section, the structure and the ice properties found in the ice patches IP1 and IP2 are discussed and compared with similar research performed on ice patches in polar (Østrem 1963; Lewkowicz and Harry 1991), subpolar (Hirvas et al. 2000; Lacelle et al. 2009; Meulendyk et al. 2012), and mid-latitude mountain environments (Wakahama and Narita 1975; Yamamoto and Yoshida 1987) (Table 2). We also explore the potential similarities with the ice properties reported for nearby cryospheric features, such as the WHIS (Ragle et al. 1964; Jeffries et al. 1991) and the northern High Arctic ice caps and glaciers (e.g., Meighen and Devon ice caps) (Koerner 1968, 1970*a*, 1970*b*; Koerner and Paterson 1974).

Ice patch stratigraphy

Both ice patches IP1 and IP2 are stratigraphically composed of two ice units, referred to as Unit 1 (upper section) and Unit 2 (lower section). Comparison of both units revealed contrasting bubbliness, sediment inclusion, and degree of fracturing (Fig. 6). In both ice patches, the transition between Unit 1 and Unit 2 is sharp and is interpreted as a melt unconformity corresponding to a relict ablation surface that developed during a period of net ablation. The melting of the upper section of the ice patches caused a concentration of sediments on the surface of the remnant ice, i.e., Unit 2 (cryoconite surface), at 135 cm depth. The resulting sediment layer was then buried by the aggradation of new ice, i.e., Unit 1. For IP1, the sediment layer cannot be observed because it corresponds to the missing core section between 130 and 140 cm depth. For IP2, the sediment layer that demarcates the unconformity is easily discernable as it represents the thickest sediment layer in the core sequence. Comparable unconformities were reported by Yamamoto and Yoshida (1987) within the Kuranosuke ice patch in the Japanese Alps.

Unit 1

The ice texture in Unit 1 typically consisted of randomly oriented, very fine (<5 mm^2) and equidimensional crystals with no evidence of interlocking patterns. It gives the ice a polygonal granular texture, typical of the ice formed from the refreezing of water-saturated snow (Koerner 1968). The ice of Unit 1 is similar to the newly formed ice sampled on IP1 and IP2 (samples IS#1, IS#2, IS#3). These observations are consistent with those reported for most of the ice patches originating from a nival system listed in Table 2. In terms of air and sediment inclusions, the ice had a bubbly ice facies and contained sporadic thin layers of suspended silt (eolian dust) as well as some compact bands of sediments including coarse particles. Such inclusions and the resulting well-developed oblique banded structure are also common to most nival ice patches (Table 2) (Østrem 1963; Lewkowicz and Harry 1991; Meulendyk et al. 2012). Based on our results and comparison with previous studies, we, therefore, propose that the bulk of Unit 1 originated from the aggradation of superimposed ice, which is the dominant process in nival ice patch systems of polar regions due to the large cold content of the ice bodies. Regionally, superimposed ice is also known to be widespread in the upper strata of Ellesmere Island ice caps (Meighen and Devon ice caps) and of the WHIS (Ragle et al. 1964; Koerner 1968; Koerner 1970*a*; Jeffries et al. 1991).

Unit 2

Unit 2 exhibits contrasting properties in terms of crystallography and ice structure compared with Unit 1 and stands out by some specificity compared with typical ice that composes nival ice patches (Table 2). Firstly, the entirety of Unit 2 is made up of medium to coarse ice crystals (15 to 20 times larger than in Unit 1, with no layer of very fine crystals.

Table 2. Summary of physical properties of the ice found in perennial and semi-permanent ice patches (modern and buried) in various environments.

Environment	System	Crystal size (mm^2)	Crystal shape	Ice facies	Bubble shape	Sediment inclusion	Structure	Fracture	Reference
Subarctic mountains	Nival	Fine (~9)	Eq/Poly	Bubble-rich	n.d.	Si	Oblique bands	no	Østrem (1963)
Mid-latitude mountains	Nival	Fine (<10)	n.d.	Bubble-rich	n.d.	Si	Oblique bands	no	Wakahama and Narita (1975)
Arctic polar desert	Nival	Fine	n.d.	Bubble-rich	Sp/Ecb/Irb	Si to Gr	Oblique bands	no	Lewkowicz and Harry (1991)
Subarctic mountains	Nival	Fine (~8)	Eq/Poly	Bubble-rich	Sp/Ecb	Si to Sa	Oblique bands	no	Meulendyk et al. (2012)
High Arctic	Nival (buried)	Very fine (~4)	Eq/Poly	Bubble-rich	n.d.	Si	Oblique bands	no	Østrem (1963)
Subarctic mountains	Nival (buried)	Medium (~14)	Eq/Poly	Bubble-rich	Sp/SSb/Ecb	Si to Sa	Oblique bands	no	Lacelle et al. (2009)
Subarctic mountains	Nival	n.d.	n.d.	Bubble-rich	Sp/Irb	Si	Oblique bands	no	Hirvas et al. (2000)
Mid-latitude mountains	Hybrid								Yamamoto and Yoshida (1987)
	Upper part	Very fine (<5)	n.d.	n.d.	n.d.	Gr	Sub-horizontal bands	no	
	Lower part	Coarse (> 100)	n.d.	n.d.	n.d.	Gr	Oblique bands	yes	
High Arctic polar desert	Nival								This study
	Upper part	Very fine (~2[a])	Ep/Poly	Bubble-rich	Sp/SSb/Irb	Si	Oblique bands	no	
	Lower part	Med. to coarse (~34[a])	n.d.	Bubble-rich/ clear ice	SSb/Ecb	Si to Gr	No clear pattern	yes	

Note: For the crystal shape: Eq, equidimensional; Poly, polygonal; Ir, irregular; El, elongated. For the bubble shape: Sb, spherical bubble; SSb, sub-spherical bubble; Ecb, elongated cylindrical bubble; Irb, irregular bubble. For sediment: Si, silt; Sa, sand; Gr, gravel. "n.d." means "no data".

[a]Values presented for this study are the average of the two ice patches studied.

Secondly, it has a low proportion of large and macro bubbles that have an elongated shape. Clear ice layers are also present. This contrasts with the bubbly ice and its whitish appearance observed in Unit 1. Finally, the presence of micro-fractures was not observed in Unit 1 and they are normally absent in ice patches originating from a nival system (Table 2).

To clarify the ambiguous origins of the ice that forms Unit 2 of both IP1 and IP2, we explore two main origin hypotheses: glacial and nival. In the hybrid system of ice patches, relict englacial ice serves as a basement for meteoric ice aggradation (Yamamoto and Yoshida 1987; Sakai et al. 2006). Even if the ice of Unit 2 shares some characteristics with englacial ice (large crystals), there are two major concerns with this interpretation. First, there is no evidence to support the presence of a glacier at WHI during the last maximum glacial extent, attained around 11 000 BP on Marvin Peninsula just south of WHI, because the severe aridity considerably limited the ice extent during the Wisconsinian (Lemmen and England 1992). Second, even if the presence of very local ice caps on WHI cannot be excluded during cold periods, as is still the case with the ice rise (Braun et al. 2004), we suggest that the ice patches most likely remained stable in size. Both investigated ice patches could not grow into glacial systems because they are topographically constrained (Glazirin et al. 2004). This hypothesis is supported by the absence of field evidence of a former greater extent of the ice patches in their frontal zones, such as protalus ramparts, pronival ridges, or moraines (Ballantyne and Benn 1994; Hedding 2016). For these reasons, the nival origin of Unit 2 is supported.

If Units 1 and 2 originate from the same processes, how to explain the difference in ice properties between them, especially regarding crystal size? Our interpretation is that two crystal growth processes, one rapid and one slow, may be involved in the formation of Unit 2.

The rapid process is related to water freezing on or within ice patches. On IP1, IS#4 collected from a supra-ice channel (Supplementary Fig. S8[2]) illustrates this process well. The refreezing of the water in the melt channels leads to the local formation of clear ice depleted in bubbles and with large and elongated crystals, similar to columnar ice (e.g., lake and pond ice; Koerner and Paterson 1974; Jeffries et al. 1991). Melt/freeze recrystallization is also involved in ice crystal growth on ice surfaces exposed to melting as demonstrated by the coarse crystals found in the weathered ice at the surface of the ice in the frontal edge of IP1 in July 2017 (Supplementary Figs. S10[2] and S11[2]). Under current conditions, these rapid ice growth processes are very localized, but they may have been more intense during past warmer periods; thus, forming sequences of coarse ice layers. This hypothesis is supported by the presence of compact layers of sediment in the ice interpreted as ablation surfaces (Fig. 6). These were often present above bands of ice with elongated bubbles that indicate the continuous expulsion of air from the supersaturated meltwater during freezing between the larger crystals. Slow freezing of water and slush accumulation in fall could also explain the layers of clear ice with coarse crystals (e.g., between 200 to 250 cm in Unit 2 of IP1; Fig. 6*a*, Supplementary Figs. S9[2] and S13[2]). Water freezing and melt–freeze recrystallization, however, did not affect all ice layers in Unit 2 because large sections show no evidence of this rapid ice growth, especially in Unit 2 of IP2 (Fig. 6*b*). Therefore, the involvement of another process must explain the coarser ice crystals.

In the absence of compressive stress, a slow steady growth of ice crystals occurs as a function of time and temperature following the normal grain growth law (Gow 1969; Cuffey and Paterson 2010). This coarsening process is driven by the reduction of the total grain boundary energy and is recognized as an important process of recrystallization of firn and ice on glaciers and polar ice caps (Gow 1969; Duval 1985; Gay and Weiss 1999; Montagnat et al. 2009). The grain size in Unit 2 of the ice patches is most likely the result of a much longer period of kinetic crystal growth. Based on this interpretation, the approximate age of Unit

Fig. 11. Vertical variation of the estimated age of the ice derived from the normal grain growth law in solid phase for Unit 2 of the ice patch (*a*) IP1 and(*b*) IP2 . The black curve represents the age profile at current ice temperature (see Fig. 9) and the blue curve represents the age profile with ice temperature 2 °C colder than today. The grey bands indicate core sections with clear ice facies where ice crystal size is partly the result of water freezing processes.

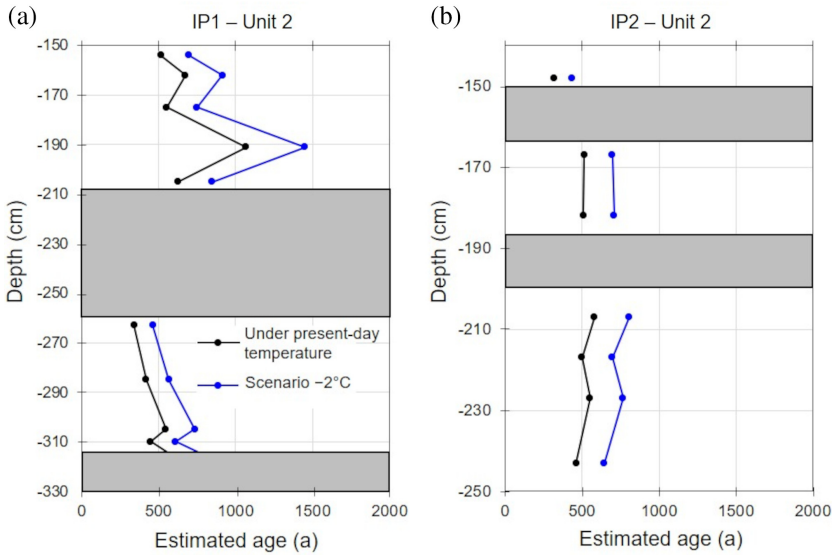

2 could, therefore, be estimated from the crystal size of the sections showing no evidence of water freezing and melt–freeze recrystallization (e.g., Supplementary Fig. S14[2]). The mean annual growth rate k ($mm^2\ a^{-1}$) was calculated using the mean monthly ice temperature measured on IP1 (Fig. 9*a*) (see Appendix E for the calculation). In Unit 2 of IP1, k was, on average, $\sim 4.8 \times 10^{-2}\ mm^2\ a^{-1}$ for July 2017 to July 2019 (Supplementary Fig. S12[2]). As the ice temperature was not measured in IP2, the same k values as for IP1 were used. Assuming that the initial ice was similar to the "young" superimposed ice that forms Unit 1, the estimated age of the ice in Unit 2 is shown in Fig. 11. In the core sections not affected by rapid ice growth, it would have taken ~500–1000 years to reach the observed average crystal sizes in the sections. This estimated age represents a lower limit of the actual age because particles and air bubbles "pin" grain boundaries and stop or at least considerably retard their motion and hence grain growth (Supplementary Fig. S14[2]; Durand et al. 2006; Cuffey and Paterson 2010). The vertical variability in crystal size along Unit 2 may be explained by different concentrations of impurities and bubbles that would lead to variations in the extent of grain boundary pinning. This explains that layers with the highest concentration in bubbles and sediments in Unit 2 generally are those with the finest crystals and, hence, the youngest apparent age. A further age underestimation can also be caused by the fact that present-day ice temperatures are likely much warmer than during the late Holocene. To evaluate the impact of colder temperature, we ran our age calculation assuming temperatures 2 °C colder and the ages were increased by ~ 250 years for the bubbly ice layers (Fig. 11).

As the hypothesis of a glacial origin has been rejected, we consider that the fractures in Unit 2 are most likely the result of the thermal contraction and cracking of the ice when it undergoes rapid temperature change that is concordant with their random orientation (Shumskii 1964, p. 305; Fortier and Allard 2005). This process is expected to occur in the

early cold season when the exposed ice surface cools rapidly before being covered by a deep snowpack (e.g., fall 2017; Fig. 9). These micro-fractures are later filled in spring by percolating meltwater which freezes rapidly to form ice veins with a high concentration in very fine bubbles (Supplementary Fig. S3[2]). These fractures are present exclusively in Unit 2, which implies that such conditions have not occurred since Unit 1 ice formed. This supports the assumption that Unit 2 would have experienced a period of strong ablation during which the ice surface was frequently exposed in late summer. Furthermore, the high frequency of fractures in Unit 2 indicates that this ice has undergone several episodes of cracking, providing further evidence that Unit 2 is much older than Unit 1.

Mechanisms of the ice formation

In this section, we propose a conceptual model for the ice growth processes and sediment incorporation in the polar ice patches (Fig. 12) based on our observations made at WHI and the existing literature. Ice patches and their seasonal snow accumulations together form a complex system in which snow and ice interact and coevolve. From this point of view, the processes involved in the aggradation of ice in ice patches are similar to what has been observed on Arctic glaciers in the so-called "superimposed ice zone" located above the equilibrium line (Koerner 1970*b*; Obleitner and Lehning 2004). Ice formation by refreezing is triggered by two distinct mechanisms that develop under different thermodynamic processes, and, hence, produce different kinds of ice. The first one is the refreezing of meltwater at the base of the snowpack over an ice mass in spring/summer to form superimposed ice and the second is the refreezing of soaked firn or weathered ice surface early in the cold season.

Superimposed ice aggradation

On WHI, as in polar regions in general, the formation of superimposed ice occurred exclusively in summer as the air temperature remains continuously below 0 °C between mid-September and mid-June (Figs. 5 and 12*a*). The ice growth starts early in the melt season during the warming phase of the snowpack (Fig. 12*b*). At this stage, the cold content of the snowpack and the underlying ice was sufficiently high that all meltwater refreezes throughout the snowpack (ice structures) and at the snow/ice interface (superimposed ice). The process, thus, consists of a mass transfer without mass loss at the scale of an ice patch system (assuming sublimation is negligible). In an advanced stage of the warming phase (Fig. 12*c*), the melting of the seasonal snowpack and snowbanks over upslope terrains can provide substantial input of meltwater into the ice patch system. As the ice patches overlie continuous permafrost (i.e., cold-based ice patch; Fig. 9) no infiltration under the ice body is possible. This meltwater is thus forced to flow on the ice surface (Ballantyne 1978). Much of this additional water is converted into superimposed ice and, thus, constitutes a net mass gain.

Assuming a high degree of wetness in the basal snow layers in the early summer, we suggest that the properties of the superimposed ice are mainly related to the size and the number density of snow grains of the original snow (Shumskii 1964, p. 295; Koerner 1970*a*). Snow grains indeed act as nuclei from which the new crystals form. This secondary ice growth is constricted to the available pore space between pre-existing snow grains. At the bottom of the seasonal snow, the shallow depth hoar layer is made of rather large and spaced out crystals so that it is expected to form a discrete (few centimetres) superimposed ice layer with fine to medium ice crystals and with large air bubbles. Above the depth hoar, the fine-grained nature of the seasonal snowpack is predisposed to form superimposed ice with very fine equiaxed, randomly oriented ice crystals, and with fine air bubbles. Due to the rapid freezing of meltwater within the cold snow, snow grain coarsening by wet

Fig. 12. Conceptual model of ice aggradation on a polar ice patch system. (*a*) Seasonal snow accumulation at the end of the cold season; (*b*) early stage of warming phase; (*c*) advanced stage of warming phase; (*d*) ripening phase; (*e*) end of the melt season after a strong ablation resulting in the complete disappearance of the seasonal snow (case 1); (*f*) end of the season after weak ablation resulting in the persistence of part of the seasonal snow layer that forms firn layer with the fall freeze-back (case 2).

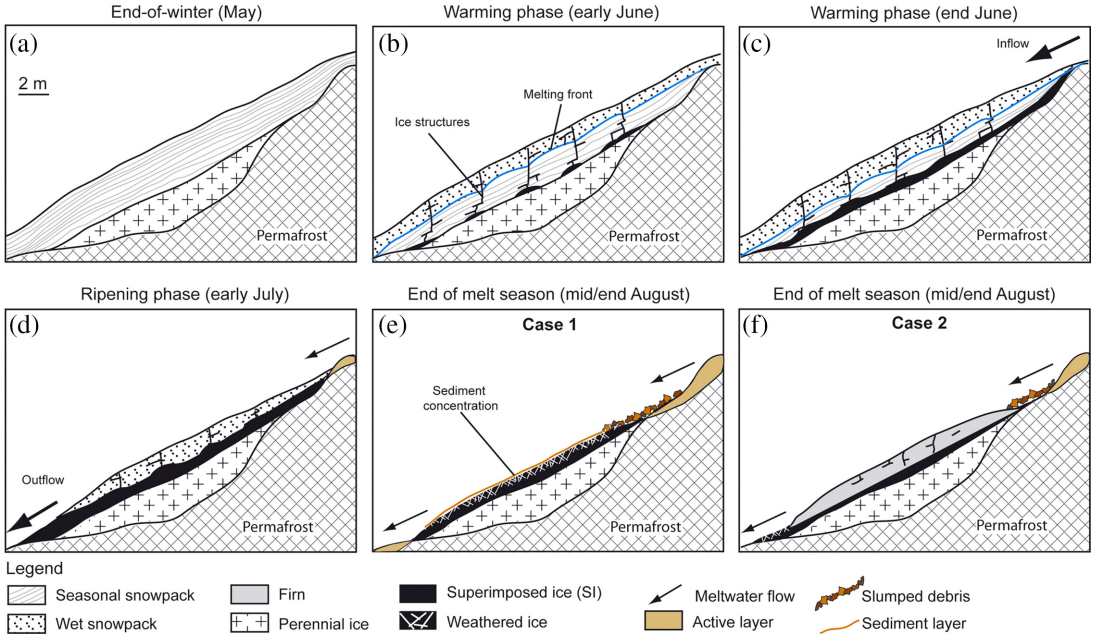

metamorphism is limited in early summer. The vertical variation of the air bubble concentration and size that forms the banded structure likely reflect short-term fluctuations in the freezing rate and the degree of soaking of the snow throughout the melt-freeze period (Lewkowicz and Harry 1991) as well as the discontinuities in the snow stratigraphy, especially the transition between the basal depth hoar layer and upper finer snow (Fig. 4).

The phase of superimposed ice aggradation is associated with the incorporation of sediments that appear suspended in the ice. This process is syngenetic when the sediments have a niveo-aeolian origin (Figs. 4, 13*a* and Supplementary Fig. S5[2]) (Lewkowicz and Young 1991). Sediment incorporation can also be epigenetic in the case of ice patches that collect upslope runoff, percolating through the snow porosity (Fig. 13*b*). Due to its fine porosity, the snowpack acts as a filter that only allows finer sediments to be transported by intranival flows (Fig. 13*c*), whereas coarser material remains temporarily trapped in the inlet at the upslope margin of the ice patches (Fig. 13*d*, *e* and Supplementary Fig. S15[2]). Because the snow-ice interface is still cold, part of this meltwater with high suspended sediment loads re-froze into superimposed ice. The filtering effect of the snowpack only occurred for a brief interval of time, because rapidly, channelled flow took place at the snow–ice interface forming slush flows and subnival pipes (Fig. 13*e*). During the ripening phase, the supra-ice streams may incise superimposed ice by thermal erosion and can carry a substantial amount of coarse and angular slope material (bedload transport) that accumulates and freezes in the ice channels (Fig. 13*f* and Supplementary Fig. S15[2]).

Conditions at WHI can sustain a long period of superimposed ice growth. First, the ice patches are covered by deep snowpacks that persist over much of the melt season and

Fig. 13. Observations of sediment deposits on ice patches IP1 and IP2. (*a*) Niveo-aeolian deposits emerging on the seasonal snow surface over IP2 in mid-June 2017; (*b*) fine-grained sediment retained in the snow porosity (filtering effect) and incorporated in the superimposed ice in the downslope edge of IP1 at the end of June 2019; (*c*) zoom in on the newly formed superimposed ice (black square in (*b*)) where entrapped fine-grained sediment are visible; (*d*) silty-sand deposits (up to 5 cm thick) in the inlet of a rill flow in the upper edge of IP1 due to snow filtering (early July 2019); (*e*) slush flow transporting silty to coarse sandy material over the ice surface of IP1 (mid-July 2019); (*f*) streamflow carved in perennial ice revealing large pebbles incorporated in blue ice (site where the sample IS#4 was collected).

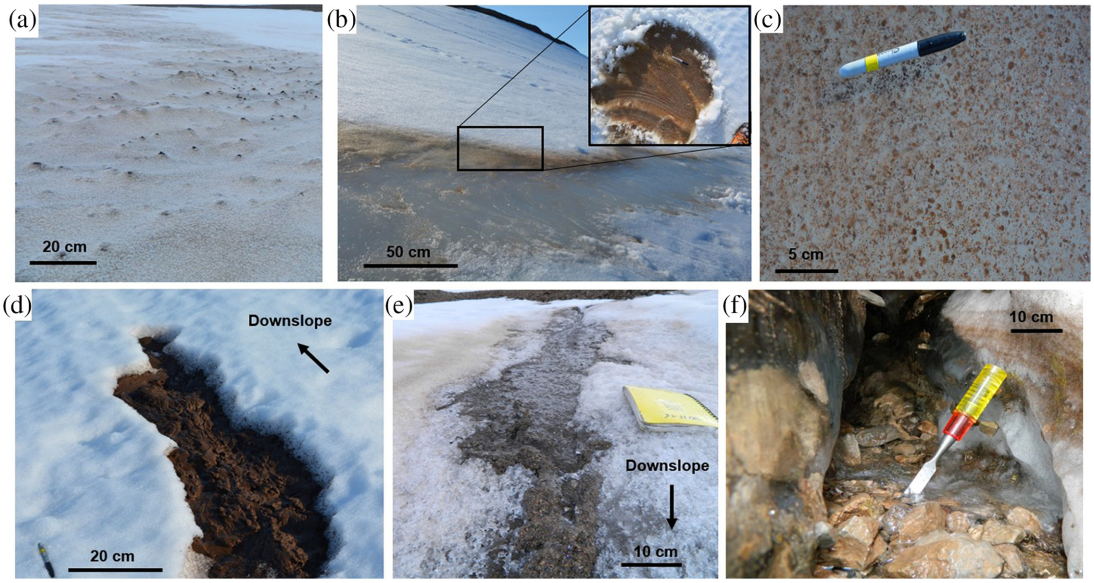

whose high density results in a high thermal inertia (Colombo et al. 2019). In summer 2017, it resulted in a lag of 18 days between the time when the air temperature turned positive and the time when the snow–ice interface reached 0 °C (Fig. 5). This lag was 21 and 20 days in June 2018 and 2019, respectively, according to borehole data (Fig. 9*b*). Second, the combination of meltwater input derived from in situ snowpack and from upslope runoff brings a high rate of water supply to the ice patch system. Third, the extreme polar winter and the cold permafrost produce low temperatures of the ice body, even under the deep seasonal snowpack (Fig. 9*b*, *c*).

During the ripening phase (Fig. 12*d*), the aggradation of superimposed ice gradually slows down as the cold content of the underlying ice surface was depleted due to latent heat absorption (Obleitner and Lehning 2004). We can estimate from the borehole data that when subsurface ice temperatures at 50 cm depth reached values close to 0 °C, the cold content of the upper layers of the ice body may have become too small to sustain the superimposed ice growth (Bøggild 2007). In summer 2017, it occurred around 25 July, namely 32 days after the snow–ice interface reached 0 °C (Fig. 9*b*). Our measurements indicated the growth of superimposed ice was rapid as approximately 30 cm of new ice was formed on 8 July. During the summer of 2018 (Fig. 9*b*), the temperature at 50 cm depth reached a brief thermal peak of—1 °C around 20 July before decreasing again so that the ice formation process likely occurred throughout the summer.

Late-season processes

Late summer conditions on ice patches are highly variable depending on the severity of ablation that will lead to the complete disappearance or not of the seasonal snow. This is critical in the ice formation processes that occur during freeze-up in the fall. Two possible scenarios have been observed (Fig. 10). In summers with significant ablation (Case 1; Fig. 12*e*), newly formed superimposed ice or old ice from previous summers is exposed at the surface as most of the snowpack has melted (e.g., summer 2017, Fig. 10*a*). Due to high levels of solar radiation and above-freezing air temperature, the exposed ice surface got weathered and formed a crust a few centimetres thick composed of porous ice with loosely interlocking crystals, whose size is generally coarse due to melt–freeze metamorphism (Supplementary Fig. S10[2]). Melting of the snowpack and superimposed ice resulted in a concentration of the sediments they contained upon the melting ice surface in the form of a thin sheet of fine material (Fig. 10*a*). Locally, coarser deposits have also formed associated with sediment inputs from the upslope section of the ice patches by small mass movements.

Conversely, when the ablation is low (Case 2; Fig. 12*f*), the end-of-summer ice patch is still covered by a significant layer of snow and the ice is only exposed at the edges (e.g., summer 2018; Fig. 10*b*). The remaining snowpack is typically composed of coarse granular snow due to prolonged wet metamorphism and the multiple freeze/thaw cycles it had undergone (Fig. 4*c*). When the soaked firn freezes at the beginning of the cold season, this results in the formation of a layer of consolidated firn (Fierz et al. 2009; Cogley et al. 2011) on top of which the new seasonal snow layer will settle (e.g., Sp1_16).

Long-term preservation of ice patches at WHI?

Although more research is needed to establish an accurate history of ice patches at WHI, some assumptions are proposed here based on our results and local paleoclimatic indicators.

Unit 2: an old basement

The ^{14}C age of ~ 3 500 years BP from a sample collected at 212–218 cm depth in Unit 2 of IP2 gives an interesting insight into the potential existence of old ice patches. This result must be considered carefully, however, because it cannot be excluded that the dated carbon was remobilized from a source of old carbon by wind or surface runoff before being deposited on the ice patch (Lewkowicz and Harry 1991). As IP2 is at the top of the slope, no runoff comes from the upslope, so all sediment layers are aeolian deposits. The dated sample included fragments of organic material of various sizes and natures (e.g., branch, flower, and moss) and from two distinct successive layers (Supplementary Fig. S4[2]), yet the ^{14}C age standard deviation is low, which suggests that the dated fragments are nearly contemporaneous. Based on the ^{14}C age and the age estimated from normal ice crystal growth law, the latter being a minimal age, we feel the most likely age is that provided by the ^{14}C dating. Regardless of the uncertainties, the ages obtained by both methods indicate the existence of old ice patches at WHI and demonstrate that ice in Unit 2 is much older than that in Unit 1. This confirms that the distinct physical properties of the ice between Units 1 and 2, and the relict ablation surface between them, reflect a hiatus in the chronostratigraphy of the ice patches.

The estimated old age of the ice patches implies their continuous existence since the late Holocene (Meghalayan 4 200 years BP to the present) and that they survived subsequent warm periods (e.g., the Medieval warm period between 1 100 to 700 years BP; Werner et al. 2018). This is consistent with other regional cryospheric and paleoclimatic records. Bradley (1990) demonstrated a decrease in summer temperature in northern Ellesmere over the last

3 500 years, which correlates with a decline in driftwood after 4 500–3 000 years BP along the northern coast of Ellesmere Island as reported by Lyons and Bielke (1973) and Koerner and Paterson (1974). This period was marked by the onset of more severe ice conditions leading to the development of ice shelves, including the WHIS (Lyons and Bielke 1973). The long-standing presence of the ice patches is also indicated by their resistance to the recent regional warming that has brought temperatures to a level not seen in the Arctic for at least 4 000 years (Lecavalier et al. 2017). The potential old age of ice patches at WHI is consistent with radiocarbon age reported for subarctic ice patches from a similar nival system existing under a warmer climate in the Northwest Territories (e.g., 4 400 years BP; Meulendyk et al. 2012) and Yukon (e.g., 4 700 years BP; Farnell et al. 2004).

A recent formation of Unit 1

With the modern climate warming that accelerated after the 1990s (Post et al. 2019), strong ablation years truncated the ancient Unit 2 of ice patches. At WHI, a major melt event could be linked to a series of warm summers from 2008 to 2012 (Supplementary Fig. S16[2]), which considerably accelerated the shrinkage of the local cryosphere. It led to the complete disappearance of the permanent ice cover on the Ward Hunt Lake for the first time in at least 60 years (Fig. 1*c*; Paquette et al. 2015), the disintegration of the WHIS (Mueller et al. 2017; Vincent and Mueller 2020), and recorded low minimum sea ice coverage (Fetterer et al. 2017). Despite a pronounced ablation, most perennial ice patches at WHI surprisingly survived these exceptional summers as shown by the GEOEYE image taken on 26 August 2011 presented in Fig. 1*c*. After 2012, the remaining ice from Unit 2 of IP1 was then buried by Unit 1 that aggraded as a result of cooler summers, especially in 2013 and 2014 (Supplementary Fig. S16[2]). Part of this newly formed ice likely melted in summer 2016, the warmest since the temperature measurements began at WHI, and the warmest year in the climate record at Alert (Fig. 1*a*). Considering that Unit 1 was still 135 cm deep when coring work was done in July 2017, we can infer that the depth of new ice formed between 2013 and 2015 probably exceeded 150–200 cm. This rapid regeneration of ice patches after a major ablation event highlights their current resilience to warm summers. The deep snowpack and upper ice layer of ice patches act as a buffer layer that is truncated during warm summers but new superimposed ice rapidly aggrades again during years with cooler summers, so that the older and deeper ice remains preserved. This cycle of strong ablation/regeneration is primarily controlled by the topography, which, in turn, controls the annual snow recharge of the system. Glazirin et al. (2004) described a regulating mechanism in which strong ablation events free up space in the topographic niche where the ice patch had formed allowing for greater accumulation of drifting snow during the following winter, and the converse. This important control of the topography and associated feedback is the key explanation for the long-term existence of the ice patches and the partial decoupling of their mass balance from the climate trend (Lewkowicz and Harry 1991; Fujita et al. 2010).

Despite their current resilience to climate change, the expected continuation of temperature warming and the increase in exceptionally warm summers could soon become critical for the preservation of the ice patches at WHI that could quickly lose their perennial status to become semi-permanent ice patches or even seasonal snow patches. This shift has already occurred farther south, at Resolute Bay (Fig. 1*a*) where the summer temperature (JJA) was 2.9 °C warmer than at WHI over the period 2006–2019 (Supplementary Fig. S13[2]) and where most of the perennial ice patches and snowbanks have completely melted after the summers of 2011 and 2012 as reported by Woo and Young (2014). At this time, it is not known what summer temperature threshold would be critical for the preservation of ice patches and how winter snow supply and summer ablation will evolve. As their

disappearance will lead to major hydrological and ecological changes in polar deserts, monitoring of the ice patches and a more detailed understanding of their current and projected functioning appears as an objective of high importance for the understanding of Arctic change.

Conclusions

This study yielded a unique data set of the physical properties of perennial ice patches in the polar desert landscape of WHI, providing new insight into the formation processes and behaviour of these small poorly studied ice masses.

Our results showed that the seasonal snowpack that accumulated on the ice patch exceeded 2 m at the end of the winter and had a high density due to the combined effect of compaction and the absence of high-temperature-gradient metamorphism. Below, the ice body was composed of two unconformable ice units with different properties in terms of ice texture and structure. The upper unit exhibited ice with fine, equidimensional ice crystals, as well as bubbly ice facies and sporadic thin layers of fine-grained sediments creating a vertical banded structure. This ice resembled, in all aspects, the superimposed ice observed in other polar and mountain ice patches as well as glaciers. The ice of the lower unit differed substantially from that of the upper ones and from the ice of typical ice patches of nival origins by the coarseness of the crystals, the lower porosity, the absence of well-defined oblique layers, inclusions of coarser sediments, and the presence of many fractures. We proposed that most of this ice was also superimposed ice with a few layers interspersed showing evidence of water or slush freezing and melt–freeze recrystallization inherited from periods of strong ablation. The coarse crystals observed in layers identified as superimposed ice suggest that the lower unit would have evolved over a long period of time by temperature-dependent crystal growth.

We have developed a conceptual model of the functioning of a snow-derived ice patch system in a cold permafrost environment. The model explains the multiple steps of ice aggradation throughout the summer and represents the interactions between snowpack, upslope input in water and sediment, and the perennial ice body. We emphasized that the properties of the seasonal snow where the superimposed ice formed, such as temperature, microstructure, density, and permeability, have a great influence on sediment retention, meltwater percolation, and the refreezing rate, which ultimately determine the texture and structure of the ice. Our results showed that the phase of the superimposed ice aggradation can last more than a month due to the high cold content of the ice and snow body that results in the formation of several decimetres of new ice every summer. In warm summers, much of the seasonal snow melts and newly superimposed ice gets exposed to melting and weathering processes. In cooler summers, a snow layer persists over most of the ice patch surface and forms a consolidated firn layer with the subsequent fall freeze-back. As such, the seasonal and interannual evolution of surface conditions of the ice patches and the ice aggradation processes involved are similar to what occurs near the equilibrium line of a polar glacier.

From the ^{14}C dating and the estimated age based on the normal crystal growth law, we inferred that the ice of the lower unit has existed continuously during most of the late Holocene period (Meghalayan 4 200 to the present). The establishment of favourable conditions for ice patch development at that time is consistent with the evolution of the climate and cryosphere on northern Ellesmere Island. With the recent climate warming that has accelerated since the 1990s, strong summer melt events became recurrent. Old ice units were, thus, probably truncated recently by a major ablation event associated with a series of warm summers between 2008 and 2012. New ice then aggraded on the old ice during a subsequent brief cooler period. This rapid regeneration of ice patches after a major ablation

event highlights their current resilience to warming due to regulating mechanisms related to topography and the ice patch shape. However, even though ice patch systems seem partially decoupled from medium- and long-term climate fluctuations, we expect that the predicted further warming will bring critical conditions for their survival, thus ending several centuries to millennia of continuous presence at WHI.

The long-term preservation of the polar ice patches identified in this study is a particularly important issue for the polar desert hydrology and the stability of the geosystem that depends on it. This question, therefore, needs to be further explored through new dating work and research on the mass and energy balance of ice patch systems to better understand their response to climate and environmental changes in the past, present, and future.

Contributors' statement

GD performed field operations, lab measurements and data analysis and wrote the manuscript. DF contributed to the sampling design, to the manuscript redaction and obtained research funding. FD contributed to the writing of the manuscript, provided inputs for data analysis and obtained funding.

Data availability statement

CT-scan images are available for download at the public data repositories of Nordicana D, managed by the Centre for Northern Studies. The complete citations for the data set are:

Fortier, D., and Davesne, G. 2021*a*. Computed tomography (CT) scans of ice cores collected in two perennial ice patches at Ward Hunt Island, Nunavut, Canada, v. 1.0 (2018–2018). Nordicana D85, doi: 10.5885/45696CE-6CC0B447C7F84E6A.

Fortier, D., and Davesne, G. 2021*b*. Snow and temperature regime of a perennial ice patch, Ward Hunt Island, Nunavut, Canada., v. 1.0 (2017–2019). Nordicana D91, doi: 10.5885/45720CE-0F556C84D96948F7.

Acknowledgements

This research was conducted with the financial support of the Natural Sciences and Engineering Research Council of Canada (NSERC), including the Discovery Frontiers project Arctic Development and Adaptation to Permafrost in Transition (ADAPT); the Networks of Centres of Excellence program ArcticNet; the Canada Research Chair program; the Northern Scientific Training Program; the Canadian Foundation for Innovation: Canadian Northern Studies Trust; Centre d'études Nordiques (CEN); and Fond de Recherche du Québec-Nature et Technologie (FRQNT). FD was supported in part by the French Polar Institute (IPEV). Logistical support was provided by the Polar Continental Shelf Program (PCSP) and Parks Canada graciously granted us the use of their facility. The authors would like to thank Karine Rioux, Audrey Veillette, and Michel Paquette for their field assistance. We also thank Maurine Montagnat for discussions on ice crystal growth. Finally, we are also grateful to the two anonymous reviewers and the editor for their insightful comments and advice on the manuscript and to Warwick Vincent for providing helpful comments on the draft manuscript.

References

Alley, R.B., and Woods, G.A. 1996. Impurity influence on normal grain growth in the GISP2 ice core, Greenland. J. Glaciol. **42**: 255–260. doi:10.3189/s0022143000004111

Bahr, D.B., and Radić, V. 2012. Significant contribution to total mass from very small glaciers. Cryosphere, **6**: 763–770. doi:10.5194/tc-6-763-2012.

Ballantyne, C.K. 1978. The hydrologic significance of nivation feature in permafrost areas. Geogr. Ann. Ser. a-Physical Geogr. **60**: 51–54. doi:10.2307/520965.

Ballantyne, C.K., and Benn, D.I. 1994. Glaciological constraints on protalus rampart development. Permafr. Periglac. Process. **5**: 145–153. doi:10.1002/ppp.3430050304.
Benson, C.S., and Sturm, M. 1993. Structure and wind transport of seasonal snow on the Arctic slope of Alaska. Ann. Glaciol. **18**: 261–267. doi:10.3189/s0260305500011629
Bliss, L.C., and Gold, W.G. 1999. Vascular plant reproduction, establishment, and growth and the effects of cryptogamic crusts within a polar desert ecosystem, Devon Island, N.W.T., Canada. Can J Bot. **77**: 623–636. doi:10.1139/b99-031.
Bøggild, C.E. 2007. Simulation and parameterization of superimposed ice formation. Hydrol. Process. **21**: 1561–1566. doi:10.1002/hyp.6718.
Bradley, R. 1990. Holocene paleoclimatology of the Queen Elizabeth Islands, Canadian High Arctic. Quat. Sci. Rev. **9**: 365–384. doi:10.1016/0277-3791(90)90028-9.
Braun, C., Hardy, D.R., Bradley, R.S., and Sahanatien, V. 2004. Surface mass balance of the Ward Hunt Ice Rise and Ward Hunt Ice Shelf, Ellesmere Island, Nunavut, Canada. J. Geophys. Res. **109**: 1–9. doi:10.1029/2004JD004560.
CEN. 2021. Climate station data from Northern Ellesmere Island in Nunavut, Canada, v. 1.3 (2002–2019). Nordicana D1. doi:10.5885/44985SL-8F203FD3ACCD4138.
Christiansen, H.H. 1998. Nivation forms and processes in unconsolidated sediments, NE Greenland. Earth Surf. Process. Landforms. **23**: 751–760. doi:10.1002/(SICI)1096-9837(199808)23:8<751::AID-ESP886>3.0.CO;2-A.
Cogley, J.G., Hock, R., Rasmussen, L.A., Arendt, A.A., Bauder, A., Braithwaite, R.J., et al. 2011. Glossary of glacier mass balance and related terms. IHP-VII technical documents in hydrology, 86: 114. [Online] Available: unesco.org/images/0019/001925/192525e.pdf.
Colbeck, S.C. 1982. An overview of seasonal snow metamorphism. Rev. Geophys. Sp. Phys. **20**: 45–61. doi:10.1002/2016GL070875.
Colombo, R., Garzonio, R., Di Mauro, B., Dumont, M., Tuzet, F., Cogliati, S., et al. 2019. Introducing thermal inertia for monitoring snowmelt processes with remote sensing. Geophys. Res. Lett. **46**: 4308–4319. doi:10.1029/2019GL082193.
Colucci, R.R., Žebre, M., Torma, C.Z., Glasser, N.F., Maset, E., Del Gobbo, C., and Pillon, S. 2021. Recent increases in winter snowfall provide resilience to very small glaciers in the Julian Alps, Europe. Atmosphere, **12**: 263. doi:10.3390/atmos12020263
Copland L., Mortimer C., White A., Richer McCallum M., and Mueller D. 2017. Factors contributing to recent arctic ice shelf losses. In Arctic Ice Shelves and Ice Islands, *Edited by* L. Copland and D. Mueller. Springer Polar Sciences. Springer, Dordrecht. doi:10.1007/978-94-024-1101-0_10.
Coulombe, S., Fortier, D., Lacelle, D., Kanevskiy, M., and Shur, Y. 2019. Origin, burial and preservation of late Pleistocene-age glacier ice in Arctic permafrost (Bylot Island, NU, Canada). Cryosphere **13**: 97–111. doi:10.5194/tc-13-97-2019, 2019.
Crabeck, O., Galley, R., Delille, B., Else, B., Geilfus, N.X., Lemes, M., et al. 2016. Imaging air volume fraction in sea ice using non-destructive X-ray tomography. Cryosphere **10**: 1125–1145. doi:10.5194/tc-10-1125-2016.
Cuffey, K.M., and Paterson, W.S.B. 2010. The physics of glaciers. Academic Press, Burlington, MA.
Davesne, G., Domine, F., and Fortier, D. 2021. Effects of meteorology and soil moisture on the spatio-temporal evolution of the depth hoar layer in the polar desert snowpack. J. Glaciol. 1–16. doi:10.1017/jog.2021.105.
De Chaumont, F., Dallongeville, S., Chenouard, N., Hervé, N., Pop, S., Provoost, T., et al. 2012. Icy: an open bioimage informatics platform for extended reproducible research. Nature Meth. 9: 690–696. doi:10.1038/nmeth.2075.
Derksen, C., Sturm, M., Liston, G.E., Holmgren, J., Huntington, H., Silis, A., and Solie, D. 2009. Northwest Territories and Nunavut snow characteristics from a subarctic traverse: implications for passive microwave remote sensing. J. Hydrometeorol. **10**: 448–463. doi:10.1175/2008jhm1074.1.
Domine, F., Cabanes, A., and Legagneux, L. 2002. Structure, microphysics, and surface area of the Arctic snowpack near Alert during the ALERT 2000 campaign. Atmos. Environ. **36**: 2753–2765. doi:10.1016/S1352-2310(02)00108-5.
Domine, F., Albert, M., Huthwelker, T., Jacobi, H.-W., Kokhanovsky, A.A., Lehning, M., et al. 2008. Snow physics as relevant to snow photochemistry. Atmos. Chem. Phys. Atmos. Chem. Phys. **8**: 171–208. doi:10.5194/acpd-7-5941-2007.
Domine, F., Belke-brea, M., Sarrazin, D., Arnaud, L., Barrere, M., and Poirier, M. 2018. Soil moisture, wind speed and depth hoar formation in the Arctic snowpack. J. Glaciol. **64**: 990–1002. doi:10.1017/jog.2018.89.
Durand, G., Weiss, J., Lipenkov, V., Barnola, J. M., Krinner, G., Parrenin, F., et al. 2006. Effect of impurities on grain growth in cold ice sheets. J. Geophys. Res. Earth Surf. **111**. doi:10.1029/2005JF000320.
Duval, P. 1985. Grain growth and mechanical behaviour of polar ice. Ann. Glaciol. **6**: 79–82. doi:10.3189/1985AoG6-1-79-82.
Environment and Climate Change Canada. 2021. National climate data and information archive. Available from http://www.climate.weatheroffice.gc.ca [accessed 15 January 2021].
Farnell, R., Hare, P.G., Blake, E., Bowyer, V., Schweger, C., Greer, S., and Gotthardt, R. 2004. Multidisciplinary investigations of alpine ice patches in southwest Yukon, Canada: Paleoenvironmental and paleobiological investigations. Arctic. **57**: 247–259. doi:10.14430/arctic502.
Fetterer, F., Knowles, K., Meier, W.N., Savoie, M., and Windnagel, A.K.. 2017 (updated daily). Sea Ice Index, Version 3. Regional Daily Data. National Snow and Ice Data Center. Available from https://nsidc.org/data/G02135/versions/3 [accessed 23 August 2020].
Fierz, C., Armstrong, R.L., Durand, Y., Etchevers, P., Greene, E., McClung, D.M. et al. 2009. The international classification for seasonal snow on the ground. UNESCO/IHP. Available from https://unesdoc.unesco.org/ark:/48223/pf0000186462 [accessed 15 August 2020].

Fortier, D., and Allard, M. 2005. Frost-cracking conditions, Bylot Island, eastern Canadian Arctic archipelago. Permafr. Periglac. Process. **16**: 145–161. doi:10.1002/ppp.504.
Fortier, D., and Davesne, G. 2021*a*. Computed tomography (CT) scans of ice cores collected in two perennial ice patches at Ward Hunt Island, Nunavut, Canada, v. 1.0 (2018-2018). Nordicana **D85**, doi:10.5885/45696CE-6CC0B447C7F84E6A.
Fortier, D., and Davesne, G. 2021*b*. Snow and temperature regime of a perennial ice patch, Ward Hunt Island, Nunavut, Canada., v. 1.0 (2017–2019). Nordicana **D91**, doi:10.5885/45720CE-0F556C84D96948F7.
Fujita, K., Hiyama, K., Iida, H., and Ageta, Y. 2010. Self-regulated fluctuations in the ablation of a snow patch over four decades. Water Resour. Res. **46**: 1–9. doi:10.1029/2009WR008383.
Gachev, E., Stoyanov, K., and Gikov, A. 2016. Small glaciers on the Balkan Peninsula: State and changes in the last several years. Quat. Int., **415**: 33–54. doi:10.1016/j.quaint.2015.10.042.
Gay, M., and Weiss, J. 1999. Automatic reconstruction of polycrystalline ice microstructure from image analysis: Application to the EPICA ice core at Dome Concordia, Antarctica. J. Glaciol. **45**: 547–554. doi:10.3189/S0022143000001416.
Glazirin, G.E., Kodama, Y., and Ohata, T. 2004. Stability of drifting snow-type perennial snow patches. Bull. Glaciol. Res. **21**:1–8.
Gooseff, M.N., Barrett, J.E., Doran, P.T., Fountain, A., Lyons, W.B., Parsons, A.N., et al. 2003. Snow patch influence on soil biogeochemical processes and invertebrate distribution in the McMurdo Dry Valleys, Antarctica. Arctic, Antarct. Alp. Res. **35**: 91–99. doi:10.1657/1523-0430(2003)035[0091:SPIOSB]2.0.CO;2.
Gow, A.J. 1969. On the rates of growth of grains and crystals in south polar firn. J. Glaciol. **8**: 241–252. doi:10.3189/S0022143000031233.
Guillet, G., and Ravanel, L. 2020. Variations in surface area of six ice aprons in the Mont-Blanc massif since the Little Ice Age. J. Glaciol. **66**: 777–789. doi:10.1017/jog.2020.46.
Haeberli, W., Frauenfelder, R., Kääb, A., and Wagner, S. 2004. Characteristics and potential climatic significance of "miniature ice caps" (crest- and cornice-type low-altitude ice archives). J. Glaciol. **50**: 129–136. doi:10.3189/172756504781830330.
Hedding, D.W. 2016. Pronival ramparts: A review. Prog. Phys. Geogr. **40**: 835–855. doi:10.1177/0309133316678148.
Hirvas, H., Lintinen, P., and Kosloff, P. 2000. An extensive permanent snowfield and the possible occurrence of permafrost in till in the RidnitSohkka area, Finnish Lapland. Bulletin-Geological Soc. Finl. **72**: 47–56. doi:10.17741/bgsf/72.1-2.003.
Jacka, T.H., and Jun, L. 1994. The steady-state crystal size of deforming ice. Ann. Glaciol. 20: 13–18. doi:10.3189/1994AoG20-1-13-18.
Jeffries, M., Serson, H., Krouse, R., and Sackinger, W. 1991. Ice physical properties, structural characteristics and stratigraphy in Hobson's Choice Ice Island and implications for the growth history of East Ward Hunt Ice Shelf, Canadian High Arctic. J. Glaciol. **37**: 247–260. doi:10.3189/S0022143000007267.
Kawamura, T. 1990. Nondestructive, three-dimensional density measurements of ice core samples by X ray computed tomography. J. Geophys. Res. Earth. **95**: 12407–12412. doi:10.1029/JB095iB08p12407.
Kawashima, K. 1993. Investigations of internal structure and transformational processes from firn to ice in a perennial snow patch. Ann. Glaciol. **18**: 117–122. doi:10.3189/S0260305500011368.
Koerner, R.M. 1968. Fabric analysis of a core from the Meighen Ice cap, Northwest Territories, Canada. J. Glacio. **7**: 421–430. doi:10.3189/S0022143000020621.
Koerner, R.M. 1970*a*. The mass balance of the Devon Island Ice Cap, Northwest Territories, Canada, 1961–66. J. Glacio. **9**: 325–336. doi:10.3189/S0022143000022863.
Koerner, R.M. 1970*b*. Some observations on superimposition of ice on the Devon Island Ice Cap, N.W.T. Canada. Geogr. Ann. Ser. A Phys. Geogr. **52**: 57–67. doi:10.1080/04353676.1970.11879808.
Koerner, R.M., and Paterson, W.S.B. 1974. Analysis of a core through the Meighen Ice Cap, Arctic Canada, and its paleoclimatic implications. Quat. Res. **4**: 253–263. doi:10.1016/0033-5894(74)90015-5.
Lacelle, D., St-Jean, M., Lauriol, B., Clark, I.D., Lewkowicz, A., Froese, D.G., et al. 2009. Burial and preservation of a 30,000 year old perennial snowbank in Red Creek valley, Ogilvie Mountains, central Yukon, Canada. Quat. Sci. Rev. **28**: 3401–3413. doi:10.1016/j.quascirev.2009.09.013.
Langway, C.C. 1958. Ice fabrics and the universal stage. U.S. Army Snow Ice and Permafrost Research Establishment, Technical Report No. 62.
Lauriol, B., Carrier, Y., Beaudet, H., and Binda, G. 1986. The residual snow cover in the Canadian Arctic in July: A means to evaluate the regional maximum snow depth in winter. Arctic, **39**: 309–315. Available from http://www.jstor.org/stable/40511027.
Lecavalier, B.S., Fisher, D.A., Milne, G.A., Vinther, B.M., Tarasov, L., and Huybrechts, P. 2017. High Arctic Holocene temperature record from the Agassiz ice cap and Greenland ice sheet evolution. Proc. Nat. Acad. Sci. 114: 5952–5957. doi:10.1073/pnas.1616287114.
Legland, D., Arganda-Carreras, I., and Andrey, P. 2016. MorphoLibJ: integrated library and plugins for mathematical morphology with ImageJ. Bioinformatics. **32**: 3532–3534. doi:10.1093/bioinformatics/btw413.
Leigh, J.R., Stokes, C.R., Carr, R.J., Evans, I.S., Andreassen, L. M., and Evans, D.J.A. 2019. Identifying and mapping very small (<0.5 km^2) mountain glaciers on coarse to high-resolution imagery. J. Glaciol. **65**: 873–888. doi:10.1017/jog.2019.50.
Lemmen, D., and England, J. 1992. Multiple glaciations and sea-level changes, northern Ellesmere Island, high arctic Canada. Boreas. **21**: 137–152. doi:10.1111/j.1502-3885.1992.tb00021.x.

Lewkowicz, A.G., and Harry, D.G. 1991. Internal Structure and Environmental Significance of a perennial snowbank, Melville Island, N.W.T. Arctic. **44**: 74–82. Available from http://www.jstor.org/stable/40511056.
Lewkowicz, A.G., and Young, K.L. 1990. Hydrology of a perennial snowbank in the continuous permafrost zone, Melville Island, Canada. Ann. Ser. A Phys. Geogr. **72**: 13–21. doi:10.1080/04353676.1990.11880297.
Lewkowicz, A.G., and Young, K.L. 1991. Observations of Aeolian Transport and Niveo-aeolian Deposition at Three Lowland Sites, Canadian Arctic Archipelago. Permafr. Periglac. Process. **2**: 197–210. doi:10.1002/ppp.3430020304.
Lyons, J.B., and Mielke, J.E. 1973. Holocene history of a portion of Northernmost Ellesmere Island. Arctic. **26**: 314–323. doi:10.14430/arctic2930.
Marsh, P. 2006. Water flow through snow and firn. *In* Encyclopedia of Hydrological Sciences. *Edited by* M.G. Anderson and J.J. McDonnell. doi:10.1002/0470848944.hsa167.
Meredith, M., Sommerkorn, M., Cassotta, S., Derksen, C., Ekaykin, A., Hollowed, A., et al. 2019. Polar regions. *In* IPCC Special Report on the Ocean and Cryosphere in a Changing Climate, *Edited by* H.-O. Pörtner, D.C. Roberts, V. Masson-Delmotte, P. Zhai, M. Tignor, E. Poloczanska, K. Mintenbeck, A. Alegría, M. Nicolai, A. Okem, J. Petzold, B. Rama, and N.M. Weyer. In press.
Meulendyk, T., Moorman, B.J., Andrews, T.D., and MacKay, G. 2012. Morphology and development of ice patches in Northwest Territories, Canada. Arctic **65**: 44–58. Available from https://www.jstor.org/stable/41638609.
Montagnat, M., Durand, G., and Duval, P. 2009. Recrystallization processes in granular ice. Low Temp. Sci. **68**(Suppl.): 81–90.
Mueller, D., Copland L., and Jeffries M.O. 2017. Changes in Canadian Arctic Ice Shelf Extent Since 1906. *In* Arctic Ice Shelves and Ice Islands. Springer Polar Sciences, *Edited by* L. Copland and D. Mueller. Springer, Dordrecht. doi:10.1007/978-94-024-1101-0_5.
Natural Resources Canada. 2019. Atlas of Canada national scale data 1:1,000,000 — boundary polygons. [Data file]. Available from open.canada.ca/data/en/dataset/fec926ca-25ad-5c92-a9a7-6009c21d17b3.
Obleitner, F., and Lehning, M. 2004. Measurement and simulation of snow and superimposed ice at the Kongsvegen glacier, Svalbard (Spitzbergen). J. Geophys. Res. Atmos. **109**: D04106. doi:10.1029/2003JD003945.
Ødegård, RS., Nesje, A., Isaksen, K., Marie Andreassen, L., Eiken, T., Schwikowski, M., and Uglietti, C. 2017. Climate change threatens archaeologically significant ice patches: Insights into their age, internal structure, mass balance and climate sensitivity. Cryosphere, **11**: 17–32. doi:10.5194/tc-11-17-2017.
Østrem, G. 1963. Comparative crystallographic studies on ice from ice-cored moraines, snow-banks and glaciers. Geogr. Ann. **45**: 210–240. doi:10.1080/20014422.1963.11881029.
Ostwald, W. 1901. Uber die vemeintliche Isomerie des roten und gelben Quecksilberoxyds und die Oberflachen-spannung Fester Korper. Z. Phys. Chem. **34**: 495–512. doi:10.1515/zpch-1900-3431
Paquette, M., Fortier, D., Lafrenière, M., and Vincent, W.F. 2020. Periglacial slopewash dominated by solute transfers and subsurface erosion on a High Arctic slope. Permafr. Periglac. Process. **31**: 472–486. doi:10.1002/ppp.2066.
Paquette, M., Fortier, D., Mueller, D.R., Sarrazin, D., and Vincent, W.F. 2015. Rapid disappearance of perennial ice on Canada's most northern lake. Geophys. Res. Lett. **42**: 1433–1440. doi:10.1002/2014GL062960.
Paquette, M., Fortier, D., and Vincent, W.F. 2018. Hillslope water tracks in the High Arctic: Seasonal flow dynamics with changing water sources in preferential flow paths. Hydrol. Process. **32**: 1077–1089. doi:10.1002/hyp.11483.
Pomeroy, J., and Brun, E. 2001. Physical properties of snow. *In* Snow ecology: An interdisciplinary examination of snow-covered ecosystems. *Edited by* H.G. Jones, J.W. Pomeroy, D.A. Walker, and R.W. Hoham. Cambridge University Press, Cambridge, pp. 45–126.
Post, E., Alley, R.B., Christensen, T.R., Macias-Fauria, M., Forbes, B.C., Gooseff, M.N., et al. 2019. The polar regions in a 2°C warmer world. Sci. Adv. **5**: eaaw9883. doi:10.1126/sciadv.aaw9883.
Ragle, R.H., Blair, R.G., and Persson, L.E. 1964. Ice core studies of ward hunt ice shelf. J. Glaciol. **5**: 39–59. doi:10.3189/S0022143000028562.
Reimer, P.J., Bard, E., Bayliss, A., Beck, J.W., Blackwell, P.G., Ramsey, C.B., et al. 2013. IntCal13 and Marine13 radiocarbon age calibration curves 0–50,000 years cal BP. Radiocarbon. **55**: 1869–1887. doi:10.2458/azu_js_rc.55.16947
Royer, A., Domine, F., Roy, A., Langlois, A., Marchand, N., and Davesne, G. 2021. New northern snowpack classification linked to vegetation cover on a latitudinal mega-transect across northeastern Canada. Écoscience, 1–18. doi:10.1080/11956860.2021.1898775.
Sakai, H., Ura, Y., Nakano, T., Iida, H., and Muroi, K. 2006. Study of the internal structure of the Kuranosuke snow patch in central Japan using ground penetrating radar survey. Bull. Glaciol. Res. **23**: 77–84.
Serrano, E., González-Trueba, J.J., Sanjosé, J.J., and Del Río, L.M. 2011. Ice patch origin, evolution and dynamics in a temperate high mountain environment: The Jou Negro, Picos de Europa (NW Spain). Geogr. Ann. Ser. A Phys. Geogr. **93**: 57–70. doi:10.1111/j.1468-0459.2011.00006.x.
Shumskii, P.A. 1964. Ground (subsurface) ice. National Research Council of Canada, Technical Translation 1130.
Stuiver, M., Reimer, P.J., and Reimer, R.W. 2021. CALIB 8.2 [WWW program]. Available from http://calib.org [accessed 28 May 2021].
Thorsteinsson, T., Kipfstuhl, J., Eicken, H., Johnsen, S. J., and Fuhrer, K. 1995. Crystal size variations in Eemian-age ice from the GRIP ice core, central Greenland. Earth Planet. Sci. Lett., **131**: 381–394. doi:10.1016/0012-821x(95)00031-7
Trettin, H.P. 1991. Geology of the Innuitian orogen and Arctic platform of Canada and Greenland. Geological Survey of Canada, Geology of Canada Series. 569p. doi:10.4095/133959.
Verpaelst, M., Fortier, D., Kanevskiy, M., Paquette, M., and Shur, Y. 2017. Syngenetic dynamic of permafrost of a polar desert solifluction lobe, Ward Hunt Island, Nunavut. Arct. Sci. **3**: 301–319. doi:10.1139/as-2016-0018.

Vincent, W.F., and Mueller, D. 2020. Witnessing ice habitat collapse in the Arctic. Science, **370**: 1031–1032. doi:10.1126/science.abe4491.
Vincent, W.F., Canário, J., and Boike, J. 2019. Understanding the terrestrial effects of Arctic sea ice decline. Eos. **100**. doi:10.1029/2019EO128471.
Vincent, W.F., Fortier, D., Lévesque, E., Boulanger-Lapointe, N., Tremblay, B., Sarrazin, D., et al. 2011. Extreme ecosystems and geosystems in the Canadian High Arctic: Ward Hunt Island and vicinity. Ecoscience, **18**: 236–261. doi:10.2980/18-3-3448.
Wakahama, G., and Narita, H. 1975. Metamorphism from snow to firn and ice in a small snow patch on Mt. Daisetsu, Hokkaido, Japan. IAHS-AISH Publ. **104**: 347–350.
Washburn, A.L. 1999. A High Arctic frost-creep/gelifluction slope, 1981–89: Resolute Bay, Cornwallis Island, Northwest Territories, Canada. Permafr. Periglac. Process. **10**: 163–186. doi:10.1002/(SICI)1099-1530(199904/06)10:2<163::AID-PPP315>3.0.CO;2-B.
Werner, J.P., Divine, D.V., Ljungqvist, F.C., Nilsen, T., and Francus, P. 2018. Spatio-Temporal variability of Arctic summer temperatures over the past 2 millennia. Clim. Past. **14**: 527–557. doi:10.5194/cp-14-527-2018.
Wilkinson, J., and Bunting, B. 1975. Overland transport of sediment by rill water in a periglacial environment in the Canadian High Arctic. Geogr. Ann. Ser. a-Physical Geogr. **57**: 105–116. doi:10.1080/04353676.1975.11879908.
Woo, A.M., Heron, R., Marsh, P., Woo, M., Heron, R., and Marsh, P. 1982. Basal ice in high arctic snowpacks. Arct. Alp. Res. **14**: 251–260. doi:10.1080/00040851.1982.12004306.
Woo, M.K., and Young, K.L. 2014. Disappearing semi-permanent snow in the High Arctic and its consequences. J. Glaciol. **60**: 192–200. doi:10.3189/2014JoG13J150.
Yamamoto, K., and Yoshida, M. 1987. Impulse radar sounding of fossil ice within the Kuranosuke perennial snow patch, Central Japan. Ann. Glaciol. **9**: 218–220. doi:10.3189/S0260305500000653.
Young, K.L., Scheffel, H.A., Abnizova, A., and Siferd, J.R. 2017. Spatial and temporal dynamics of groundwater flow across a wet meadow, Polar Bear Pass, Bathurst island, Nunavut. Permafr. Periglac. Process. **28**: 405–419. doi:10.1002/ppp.1931.
Zhao, B., and Wang, J. 2016. 3D quantitative shape analysis on form, roundness, and compactness with μCT. Powder Technol. **291**: 262–275. doi:10.1016/j.powtec.2015.12.029.

Appendix A

Snow pits

All snowpits were dug down to the perennial ice surface. For each of them, a snow face was opened about 1.5 m wide where the measurements were made. The snow stratigraphy and the physical properties (density, grain size and shape, and temperature) were analyzed in situ following the procedure of Fierz et al. (2009) and Domine et al. (2018). The snow density (ρ_s, kg m^{-3}) was measured by collecting snow samples with a 10 cm vertical resolution using a metal cylinder of 224.1 cm^3 for horizontal sampling (7 cm in diameter). The samples were weighed in the field with an electronic high-precision scale (resolution: 0.1 g). The mass was then converted into density. Snow temperature was measured at the same vertical resolution as density using a handheld thermistor thermometer HH41 (uncertainty ± 0.015 °C; resolution 0.01 °C; Omega®). The average grain size (E, in mm) and shape were determined in the field by placing a sample of snow on a black millimetre-gridded crystal card and examining it with an 8× magnifying glass.

Appendix B

Drilling procedure

The ice cores were retrieved using a 75 mm inner diameter SIPRE-corer driven by a Stihl® powerhead. The coring was made vertically. The SIPRE-corer was able to drill through bands of ice with a high content of fine-grained sediments. When a drilling refusal occurred because of a coarser sediment layer (i.e., gravel, blocky material), the SIPRE-corer was changed to an 82.5 mm diamond carbide core barrel. The bottom of the ice patches was considered to be met when the corer extracted large pieces of rock or frozen soil interpreted as the bed of the ice patch.

Appendix C

Thin section procedure

Thin sections were prepared from 10 mm thick slices of ice cut horizontally, every 10 cm, and vertically, every 20 cm, in the ice cores using a band-saw. For the ice samples, IS#1 to IS#4, four thin sections per sample were made. Ice slices were then frozen on glass plates of 10 cm^2 by injecting droplets of near-freezing water on the edges of the samples to create a thin ice bond. The last step consisted of thinning the ice slices to 0.2–0.5 mm using a manually driven microtome (Leica™). The thin sections were then placed between two cross linear polarizing filters illuminated from below by a light table. Due to the birefringence (i.e., double refractivity) of the ice crystals and their variable c-axis orientation along which the light is transmitted, individual ice crystals appear in different colors and brightness.

The thin sections were first photographed with transmitted light to detect the gas/sediment inclusions and fractures. Then, they were photographed under cross-polarized light to reveal crystals. A single image is often not sufficient to clearly distinguish all individual crystals because an individual crystal could remain dark for a certain angle and be illumined from another (Gay and Weiss 1999). For this reason, a total of 5 cross-polarized pictures were taken at 0°, 45°, 90°, 135°, and 180° while the thin section stayed fixed with respect to the camera. The post-processing step consisted of automatically detecting the crystal boundaries using the open-source imaging software ImageJ (Fig. 3). A semi-automatic segmentation, based on watershed flooding algorithms, was performed using the ImageJ plugin MorphoLib (Legland et al. 2016). The high resolution of the photography allows the detection of crystals as small as 0.2 mm. The output raster files of grain boundary networks were converted to shapefile (polygons) in ArcGIS (Esri™) and then manually cleaned when necessary. The main error inherent to the automatic detection of crystal boundaries is the clustering of contiguous crystals in the same polygon when they appear in the same color tone (similar c-axis orientation). In this case, a careful analysis of the thin section with the naked eye allows applying a correction. When contiguous crystals have their c-axis perpendicular to the thin section, they remain dark whatever the viewing angle. In this case, the best way to reduce the error is to remove them as suggested by Gay and Weiss (1999). The corrected images are then re-imported to ImageJ and the two-dimensional morphometrics properties of the ice crystals that compose a thin section were computed. The size of each crystal was measured by the surface area (A, in mm^2) and the major axis length (L, in mm). The shape (elongated, rounded, and subrounded) of the crystals was analyzed by computing the roundness parameter (R), which takes into consideration the major axis of the best fit ellipse (eq. (C1)) (Zhao and Wang 2016). The lower the value, the more elongated the shape.

$$R = 4 \times \frac{A}{\pi \times L^2} \quad \text{(C1)}$$

Appendix D

CT-scan technology and image analysis

CT-scans were obtained by a Siemens Somatom 64 scanner at the Institut National de la Recherche Scientifique (INRS-ETE) in Québec City, Québec Canada. This is a non-destructive tool that preserves the integrity of the sample. This technique has already been used to analyze lake ice, sea ice (Crabeck et al. 2016), and permafrost (Coulombe et al. 2019). The cores

were scanned from top to bottom, providing transverse and longitudinal slices images that create a three-dimensional "stack" of images after compilation. The pixel resolution of each horizontal (X) and vertical (Y) image was 0.195 × 0.195 mm giving a two-dimensional pixel resolution of 0.038 mm^2. Each slice integrated a thickness (Z) of 0.4 mm, making the voxel resolution of 0.0152 mm^3. The output of the scanning is a set of DICOM 16-bit greyscale images representing a 3D reconstruction of the cores with a high degree of accuracy. The pixel value, expressed in Hounsfield units (HU), represents the linear attenuation of the X-ray, which depends on the density of the material. Lower density materials (i.e., gas) appear in darker tones, whereas lighter tones indicate higher density material (i.e., ice and sediments).

The processing of the images first consisted of converting them into binary images. The manual adjustment of the segmentation threshold made it possible to detect air bubbles larger than 0.2 mm in diameter (Crabeck et al. 2016). It provided a high-resolution sub-millimetre profile of the air fraction, expressed by the porosity (ϕ in %) for a given volume of ice (V). Then, the bulk density (ρ_i, kg m^{-3}) of the ice was calculated using eq. (D1) (Kawamura 1990):

(D1) $$\rho_i = (100 - \phi)\rho_{i,p}$$

where $\rho_{i,p}$ is the density of the pure ice (free of air and sediment) at 0 °C (916.8 kg m^{-3}). The values of bulk density derived from CT images were then validated with laboratory measurements based on weighing samples of known volume. We found good agreement between both methods (Supplementary Fig. S2[2]).

Appendix E

Calculation of ice crystal kinetic growth

A mixture of grains with a given size distribution evolves naturally, the driving force being the reduction of interface energy. This process has been documented for grains in a solvent or air where it is known as Ostwald ripening (or coarsening) (Ostwald 1901). Interface energy minimization also applies to a solid formed of grains such as ice in ice sheets (Durand et al. 2006). In the absence of non-hydrostatic stress, ice crystals grow by recrystallization following a temperature-dependent rate (Gow 1969). This normal grain growth law to describe this process is expressed by (Cuffey and Paterson 2010):

(E1) $$A = A_0 + kt$$

where A is the mean surface area of crystals (mm^2) at time t; A_0 is the initial surface area; k is the growth factor (mm^2 a^{-1}), which has an Arrhenius temperature dependence. Considering that the initial ice is superimposed ice, we assumed A_0 is equal to the average value of crystal size found in Unit 1. k was calculated as follows (Cuffey and Paterson 2010):

(E2) $$k = k_0 e^{-Q/RT}$$

where Q is the activation energy, k_0 is the pre-exponential factor, R is the gas constant (8.314 j $K^{-1}mol^{-1}$) and T is the absolute temperature (Kelvin). The activation energy is generally inferred by plotting ln(k) as a linear function of $1/T$. Compilation of published values of k reported by Duval (1985), Jacka and Jun (1994) and Cuffey and Paterson (2010) gives a constant value for the activation energy of ~51 kJ mol^{-1} for the range of temperature −4 to −50 °C (Fig. E1). At ~ −4 °C, a break occurs in the linear relation of ln(k) with $1/T$ due to a

Fig. E1. Plot of the ice crystal growth factor (k, mm^2 a^{-1}) in a logarithmic scale as a function of 1/T. Data were obtained by field and laboratory experiments by Jacka and Jun (1994); Duval (1985); and Cuffey and Paterson 2010. Below –4 °C (green vertical line), the blue linear regression line was used to obtain the activation energy (Q).

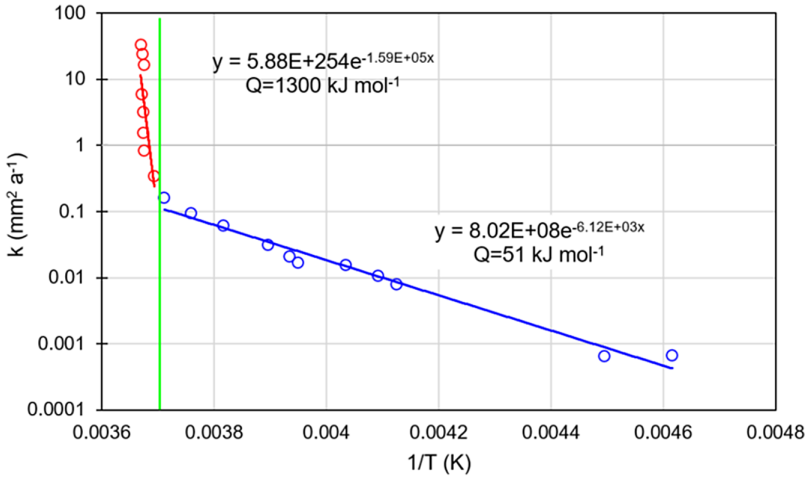

drastic increase of Q when the temperature approaches the melting point (Jacka and Jun 1994. In this study, we postulate that the temperature of the lower units of the ice patches remained below –4 °C as indicated by the thermal regime of the ice body below 150 cm depth (Fig. 9*a*).